Repetitive Neuronal Activation Regulates Cellular Maturation State via Nuclear Reprogramming

Tomoyuki Murano[1], Hideo Hagihara[1], Katsunori Tajinda[2], Keizo Takao[3,4], Yoshihiro Takamiya[1], Kaoru Katoh[5,6,7], Alfred J. Robison[8], Mitsuyuki Matsumoto[9], Masakazu Namihira[5], Tsuyoshi Miyakawa[1]*

[1]Division of Systems Medical Science, Center for Medical Science, Fujita Health University, Toyoake, Japan
[2]Astellas Research Institute of America, San Diego, CA, USA
[3]Department of Behavioral Physiology, Faculty of Medicine, University of Toyama, Toyama, Japan
[4]Research Center for Idling Brain Science, University of Toyama, Toyama, Japan
[5]Biomedical Research Institute, National Institute of Advanced Industrial Science and Technology (AIST), Tsukuba, Japan
[6]Artificial Intelligence Research Center, National Institute of Advanced Industrial Science and Technology (AIST), Tsukuba, Japan
[7]Ph.D. Program in Humanics, School of Integrative and Global Majors, University of Tsukuba, Tsukuba, Japan
[8]Department of Physiology and Neuroscience Program, Michigan State University, Michigan, USA
[9]Arialys Therapeutics Inc, La Jolla, CA, USA

***Correspondence:**
Tsuyoshi Miyakawa
Division of Systems Medical Science, Institute for Comprehensive Medical Science, Fujita Health University, 1-98 Dengakugakubo, Kutsukake-cho, Toyoake, Aichi 470-1192, Japan
Telephone: +81-562-93-9376
Fax: +81-562-92-5382
E-mail: miyakawa@fujita-hu.ac.jp

Abstract

Neural stimulation, such as electroconvulsive therapy (ECT) and repetitive transcranial magnetic stimulation (rTMS), are highly effective clinical interventions for a broad spectrum of psychiatric disorders, including depression and schizophrenia. However, their mechanism of action at the cellular level remains poorly understood. Here, we modelled ECT with repeated optogenetic neuronal stimulation in the mouse dentate gyrus, and observed ECT-like behavioral effects, including decreased depression-like behavior and increased locomotor activity. At the cellular level, we found dematuration to a long-term stable state, persisting for more than one month, defined by changes in nuclear structure, gene expression patterns resembling the G_2/M phase of the cell cycle, and altered neural coding of navigational information. Moreover, knockout of the G_2/M master regulator Cyclin B rescued some of behavioral and cellular effects. These findings demonstrate that ECT-like brain stimulation triggers plasticity of the cellular state, revealing a form of stimulus-regulated nuclear reprogramming with potential clinical utility.

Introduction

In the adult mammalian brain, strong synchronous neural activity typically has toxic effects on neuronal function and viability. Cumulative electrical activity of sufficiently high amplitude, frequency, and/or duration interferes with cellular metabolism, flooding cells with excess calcium and resulting in metabolic failure and death[1,2]. High-intensity neural activity also results in maladaptive neuronal changes, such as dendritic spine loss[3,4], abnormal neurite arborization[4,5], and toxic excitability[6]. Previous studies have identified an intermediate state of senescence after overactivation, characterized by the dematuration of adult neurons to an immature-like state, including global de-differentiation of gene expression patterns, membrane excitability, and neural plasticity[7–11]. Similar neuronal phenotypes have been observed in genetically engineered mice that exhibit abnormal behaviors mirroring common neuropsychiatric disorders, such as schizophrenia, intellectual disability, and bipolar disorder[7,12–16]. Our recent study investigated the levels of lactate, a surrogate marker of neural excitation, in the brains mouse models relevant to neuropsychiatric disorders, and found all mouse models with immature brain phenotypes investigated in this study showed significant increases in lactate levels, suggesting a potential link between cellular hyperexcitability and the immature phenotype[17]. Additionally, immature-like gene expression patterns have been identified in the brain tissues of human patients with neuropsychiatric disorders, such as epilepsy, Alzheimer's disease, and schizophrenia[11,18–23], where neural hyperexcitability is a known or suspected etiological contribution.

In marked contrast to the detrimental effects of high-intensity neural activity, there are reported beneficial effects of moderate electrical activity on neural circuit function. Neural activity is essential for brain development, learning and memory[24,25], including enhancements in synaptic weight[26,27], neuronal excitability[28,29], and gene expression[30,31]. An interesting clinical application of moderate activity is the use of electrical brain stimulation technologies such as electroconvulsive therapy (ECT), as a class of methods for ameliorating negative symptoms in patients with major depression[32,33]. ECT promotes neuroplastic changes, such as increased adult neurogenesis in the dentate gyrus and hippocampal volume enlargement[34–36] with 6–12 repeated stimulations commonly used for long-term positive clinical outcomes[32,33]. Electroconvulsive stimulation (ECS), the animal equivalent of ECT, also induces molecular and electrophysiological changes, such as enhanced neurogenesis and altered synaptic transmission[9,14,37,38]. Similar changes occur with chronic administration of fluoxetine, a selective serotonin reuptake inhibitor (SSRI)[9,39,40]. Interestingly, repetitive ECS and chronic fluoxetine administration can induce cellular dematuration, suggesting that unspecified cellular plasticity may underpin their antidepressant effects[9,39–41] Likewise, other noninvasive brain

stimulation methods, such as repetitive transcranial magnetic stimulation (rTMS) and transcranial direct current stimulation (tDCS), can induce neuroplastic changes in the brain and have promising therapeutic potential [42,43]. However, despite their common use, the specific cellular mechanisms engaged by these brain stimulation therapies, including clinical ECT, rTMS, and tDCS, remain poorly understood.

In this study, we aimed to elucidate the primary cellular mechanisms by which brain stimulation technologies like ECT cause cellular dematuration. We applied an ECT-like optogenetic stimulation to granule cells of the hippocampal dentate gyrus, a key brain area for ECT, to produce clinically relevant behavioral effects. This stimulation led to an immature-like gene expression profile in the brain of mice, and a similar patten was observed in the post-mortem brains of patients with mood disorders. Our analysis also revealed that repetitive stimulations induce G_2/M cell cycle re-entry and nuclear structural plasticity with epigenomic and morphonuclear signatures. These findings reveal a unique immature cellular state induced by ECT-like neuronal activation, which has long-term stability, and a mechanism of activity-dependent nuclear reprogramming, offering mechanistic insight into ECT effects and related applications.

Results

1. *Neuronal activations trigger an immature cellular state in DG granule cells*

We challenged neurons *in vivo* with a stimulation protocol designed to mimic human ECT, in which seizure duration is a critical determinant of therapeutic efficacy and is therefore tightly controlled in clinical settings. Conventional methods, such as seizure-inducing drugs and animal ECS, do not allow precise control over seizure duration, leading to variability in cellular and network-level effects. To overcome this limitation, we used mice expressing channelrhodopsin-2 (ChR2) in granule cells (GCs) of the dentate gyrus (DG) (POMC-Cre::ChR2-EYFP mice) and applied optogenetic stimulation, termed Repetitive Optogenetic Stimulation (REPOPS), enabling precise control over the frequency and duration of stimulation (Fig.1a and Extended Data Fig. 1a). This optogenetic approach allowed us to establish a precise experimental system to study cellular effects confined to a specific target cell population. We employed a moderate stimulation protocol that did not cause cell death (Extended Data Fig. 1b–d).

REPOPS was performed either three or ten times consecutively (Fig. 1a). The expression of calbindin (CB), a maturation marker of GCs, was reduced 24 hours after REPOPS for three days, but returned to a level that was not significantly different from the pre-stimulus levels within two weeks (Fig. 1b). In contrast, REPOPS for 10 days significantly decreased CB expression at 24 hours and two weeks after the last stimulation (Fig. 1b). The decrease in CB was inhibited by the administration of Ca^{2+} blockers (Extended Data Fig. 2a–c), suggesting that Ca^{2+} influx is crucial for REPOPS-induced dematuration. RNA-seq analysis showed that the number of genes with significant changes in expression ($P < 0.05$, fold change > 1.2; vs. No Stim group) decreased over time after 3-day REPOPS, but remained unchanged after 10-day REPOPS (Fig. 1c). Evidently, neuronal activation repeated a few times induces short-term transcriptome changes that spontaneously revert to the original state; however, when neuronal activation is chronically repeated, the changes are sustained for longer periods. To examine whether REPOPS induces an immature-like gene expression pattern at the transcriptome level, we assessed the similarity between gene expression patterns of optogenetically-stimulated DG and those of normal infant mice (GSE113727[11]) by the Running Fisher test[44], a rank-based nonparametric algorithm that evaluates the degree of overlap between two gene groups implemented in BaseSpace (Illumina, Cupertino, CA, USA). There was a striking degree of similarity between the datasets (Overlap $P = 3.9 \times 10^{-52}$) with the same directional changes in expression (Fig. 1d). Collectively, these results indicate that REPOPS for 10 consecutive days induces long-lasting immature-like gene expression patterns in the DG, whereas REPOPS for three days does not.

As REPOPS was designed to model the effects of human ECT, we next asked whether ECT in human patients also induces an immature-like gene expression pattern. We reanalyzed RNA-seq data from the post-mortem DG of bipolar disorder and major depressive disorder patients with and without ECT (SRP241159[45]). Genes differentially expressed between ECT-treated and non-ECT-treated patients were compared with those changing during typical hippocampal development (0–5 months vs. 20–39 years; GSE25219[46]). This analysis revealed a significant overlap between the two datasets (Overlap $P = 1.2 \times 10^{-8}$), with consistent directional changes (Fig. 1f), suggesting that ECT induces an immature-like gene expression pattern in the DG of human patients, in line with the pattern observed in REPOPS. Notably, both REPOPS and human ECT induced long-term alterations in the expression of synapse-related genes: REPOPS significantly downregulated *Gria1*, *Gria2*, *Camk2a*, and *Camk2b*, and upregulated *Arc* (Fig. 1e), while ECT-treated patients exhibited similar alterations in GRIA1, GRIA2, and ARC compared with non-ECT-treated patients (Fig. 1g), suggesting a shift toward an immature synaptic state.

2. *REPOPS regulates the long-term plasticity of genomic structure*

Changes in gene expression are often accompanied by alterations in the chromatin structure of the associated genomic regions[47]. To investigate whether and how neural overactivation alters the chromatin accessibility of neurons, we performed ATAC-seq on optogenetically stimulated DG tissue (Fig. 1h). Volcano plots showing changes in chromatin accessibility are shown in Fig. 1i. We found significant changes in chromatin accessibility in 806 chromatin regions (748 opened and 58 closed) and 21,853 chromatin regions (15,098 opened and 6,755 closed) in the Stim×3+2wks and Stim×10+2wks groups, respectively (Fig. 1i). These results indicate that repeated neuronal activation for 10 consecutive days, but not for 3 days, induced widespread and persistent reorganization of three-dimensional genome structure, along with concordant global transcriptome changes.

3. *REPOPS initiates long-term anti-depressive behavioral changes in mice*

To assess whether ECT-like neuronal activation could alter anti-depressive behavior, we first performed an open field (OF) test (Fig. 2a, 2b). Locomotor activity was recorded for 30 min each day, and the dorsal DG was optogenetically stimulated for 5 min (20–25 min after the start) on each stimulation day. As previously reported[48], mice showed an increase in locomotor activity immediately after stimulation (a1–a3 in Fig. 2a). Interestingly, on the day after the first stimulation, mice in both Stim×3 and Stim×10 groups exhibited a significant increase in distance traveled during the first 15 min compared to the No Stim group ($P = 0.0134$,

169 Day 2 in Stim×10 group; $P = 8.05 \times 10^{-4}$, Day 9 in Stim×3 group; Fig. 2b). In the Stim×3
170 group, this increase peaked on Day 9 and returned to control levels within two weeks (blue line
171 in Fig. 2b), whereas in the Stim×10 group, it declined gradually from the last stimulation day
172 but remained significantly elevated two weeks after the last stimulation (Day 24, $P = 0.00362$;
173 red line in Fig. 2b). Thus, neuronal activation of the DG repeated for 10 days induced
174 hyperlocomotor activity persisting for at least two weeks, whereas an increase in locomotor
175 activity after neuronal activation for three days was transient. We also conducted 24-hour
176 activity monitoring in the home cage (Fig. 2c). The distance traveled by mice in the Stim×10
177 group gradually increased after the initial stimulation and was significantly higher than that in
178 the No Stim and Stim×3 groups ($P < 0.05$, Days 7–36; Fig. 2c). Mice in the Stim×3 group did
179 not show any significant increase in locomotor activity in the home cage. These results indicate
180 that repeated neuronal activation causes a significant increase in baseline locomotor activity,
181 which persists for more than one month. Depression-related behavior was assessed with the
182 tail suspension test (Fig. 2d). Mice in the Stim×10 group showed significantly less immobility
183 compared to those in the No Stim ($P = 0.0094$) and Stim×3 groups ($P = 0.0198$). A similar
184 trend was observed in the forced swim test (Fig. 2e), where Stim×10 mice showed reduced
185 immobility compared to the No Stim group ($P = 0.0304$) and Stim×3 group ($P = 0.0770$). These
186 results suggest that repeated neuronal activation mimicking ECT reduces depression-like
187 behavior in mice (for other behavioral tests, see also Extended Data Fig. 3).
188
189 **4. *Alterations of neural coding of navigational information***
190 To investigate whether and how neural overactivation affects circuit function, we
191 performed *in vivo* Ca^{2+} imaging under freely moving conditions combined with optogenetic
192 stimulation (Fig. 3a, 3b). On each stimulation day, we recorded DG neuron activity and
193 locomotor activity in the OF during the first 30 min, followed by 5 min of optogenetic
194 stimulation (590–650 nm, 20 msec pulse, 10 Hz; Fig. 3c). The distance traveled during the first
195 30 min in the Stim×10 group gradually increased and was significantly greater than in the No
196 Stim group two weeks after the last stimulation ($P = 0.0358$; Fig. 3d). However, the mean Ca^{2+}
197 transient rate did not differ significantly between these groups throughout the experiment (Fig.
198 3e).
199 Navigational information, such as position and speed, is encoded in the population
200 activity of DG neurons[16,49]. To examine how neural overactivation affects this coding, we
201 computed spatial and speed information for individual DG neurons. In the No Stim group,
202 spatial information increased on Days 2–11 and Days 24–26 compared to Day 1 (Cohen's d =
203 0.43 and 0.30), suggesting that OF exposure enhanced spatial coding (Fig. 3f). In contrast, the

Stim×10 group showed reduced spatial information on Days 2–11 and Days 24–26 compared to the No Stim group (d = –0.50 and –0.45; Fig. 3f). Speed information remained unchanged in the No Stim group throughout the experiment ($|d| < 0.10$), but increased in the Stim×10 group on Days 2–11 and Days 24–26, exceeding that in the No Stim group (d = 0.46 and P = 0.63; Fig. 3i). Thus, repeated neuronal activation reduced spatial coding and enhanced speed-related activity in individual DG neurons for over two weeks.

To examine information encoding at the population level, we predicted mouse position and speed from the population activity of DG neurons using machine learning methods. Representative decoding results are shown in Fig. 3g and 3j. In the No Stim group, position decoding errors decreased on Days 2–11 and Days 24–26 and were significantly smaller than chance (Fig. 3h). In contrast, the Stim×10 group showed no significant change in position decoding accuracy, and decoding errors were significantly greater than in the No Stim group on Days 2–11 and Days 24–26 (P = 0.0133 and 0.0335; Fig. 3h). These findings suggest that position information coding was enhanced by OF exposure but impaired by neural overactivation. Speed decoding accuracy did not change significantly during the experiment in the No Stim group, but was increased by REPOPS in the Stim×10 group and was significantly higher than in the No Stim group on Days 2–11 and Days 24–26 (P = 0.0363 and 0.0223; Fig. 3k). Thus, repeated neuronal activation reshapes information processing in the DG by suppressing spatial map formation and enhancing speed-related activity, with unchanged overall activity levels. This shift may underlie the behavioral changes observed in optogenetically stimulated mice, such as increased locomotor activity and reduced depression-like behavior.

5. *REPOPS-driven long-term increases in the expression of cell cycle-related genes*

We next explored potential molecular markers associated with REPOPS-induced neuronal alterations by conducting gene ontology analysis of RNA-seq data from optogenetically-stimulated DG. Notably, gene categories significantly altered in the Stim×10+2wks group—but not in the Stim×3+2wks group—included cell cycle–related terms, such as *"cell division"* and *"mitotic cell cycle process"* (Extended Data Fig. 4). Expression levels of representative cell cycle-related genes are shown in Fig. 4a. Genes related to the G_2/M phase, such as *Ccna2*, *Ccnb1*, *Ccnb2*, and *Cdc25c*, were significantly increased in Stim×10+2wks compared to the No Stim group, whereas genes related to other phases, such as *Ccne1*, *Ccne2*, *Cdk2* (G_1-S phase), and *Ccnd1*, *Cdk4* (G_1 phase), showed no significant changes (Fig. 4a). We found that cyclin B, an essential regulator for the transition from G_2 to M phase, was expressed in most DG neurons in Stim×10+2wks, while it was barely detectable in the No

239 Stim group (Fig. 4b). It was broadly expressed throughout the granule cell layer and was not
240 restricted to the subgranular zone, where newborn neurons are abundant, indicating that the
241 majority of cyclin B expression reflects induction in mature neurons, rather than enhanced
242 neurogenesis.

243 To assess whether gene expression patterns induced by REPOPS resembled specific
244 cell cycle phases, we used a publicly available microarray dataset of HeLa cells that captures
245 gene expression pattern dynamics throughout the cell cycle (Fig. 4c; GSE3497[50]). In this
246 dataset, genes characteristic of each phase were identified through microarray analysis of HeLa
247 cells sampled at multiple time points across the cell cycle. We compared these cell cycle phase-
248 specific gene lists (1–30 hour from S phase) with RNA-seq data from optogenetically
249 stimulated DG (Fig. 4c) and computed a "similarity score" for each time point, defined as the
250 $-\log_{10}$ of the overlap *P* value (Fig. 4d). In Stim×3+24hrs and Stim×10+24hrs, similarity score
251 peaks were observed at 7, 8, and 20 hours from S phase (scores > 3.0; Figs. 4d), corresponding
252 approximately to the G_2/M phase. In Stim×3+2wks, these peaks declined (scores < 2.0),
253 whereas in the Stim×10+2wks group, they remained elevated (scores > 3.0; Figs. 4d). Although
254 neurons are considered post-mitotic and do not undergo cell cycle progression, these findings
255 suggest that repeated neuronal activation reinstates G_2/M phase-like transcriptional programs
256 in mature neurons that persist for over two weeks.
257

258 **6. *Long-term G_2/M phase-like epigenomic plasticity in nuclear structure***

259 We investigated whether REPOPS can induce changes in nuclear structure, focusing
260 on three major events that occur during the G_2/M phase: (i) nuclear lamina disruption, (ii) an
261 increase in the phosphorylation of histone H3 (pH3), and (iii) chromatin condensation.

262 (i) The nuclear lamina is a dense fibrillar network lining the inner nuclear membrane
263 and providing mechanical support for chromatin organization, which disrupts during mitosis
264 due to nuclear division[51,52]. In the No Stim group, most neurons exhibited normal, round-
265 shaped lamin B1, the main component of the nuclear lamina (Fig. 4e and Extended Data Fig.
266 5a, 5b). In contrast, neurons in the Stim×10+2wks group showed varying degrees of reduced
267 expression and/or disrupted lamin B1 structure, indicating that 10 days of REPOPS induced
268 nuclear lamina disruption (Fig. 4e).

269 (ii) Increased phosphorylated histone H3 (pH3) is another characteristic change
270 during mitosis, which is a known "mitosis marker." In the No Stim group, most neurons showed
271 minimal immunoreactivity of pH3, whereas the Stim×10+2wks group exhibited a significant
272 increase in pH3 immunoreactivity (Fig. 4f), suggesting that repeated neuronal activation
273 induces mitosis-like epigenetic modifications of chromatin in mature neurons.

274 (iii) The chromocenter is an aggregation of heterochromatin domains, which can be
275 visualized as concentrated dot-like signals in the nucleus by DNA counterstaining (indicated
276 by red arrowheads in Fig. 4g). It is considered a central site for chromatin condensation during
277 mitosis[53,54]. The chromocenter ratio–defined as the ratio of total chromocenter area to the
278 nucleus size–was significantly increased by REPOPS, indicating an enlargement of
279 heterochromatin domains (Fig. 4g). Thus, REPOPS induces a G_2/M phase-like nuclear states,
280 characterized by nuclear lamina disruption, increased pH3, and chromatin condensation (see
281 also Extended Data Fig. 6a, 6b).
282
283 **7. *Cyclin B mediates REPOPS-induced changes in nuclear structure, cellular immaturity,***
284 ***and behavior***
285 To investigate the molecular mechanisms underlying G_2/M phase-like nuclear
286 alterations, we knocked out the expression of cyclin B–an essential gene for the G_2/M phase
287 transition–by injecting a mixture of AAV9-SpCas9 and AAV9-sgRNA encoding sequences
288 targeting *Ccnb1* and *Ccnb2* (CyclinB-KO) into the DG (Fig. 5a, 5b). AAV9-sgRNA encoding
289 scrambled sequences (Scram-KO) was used as a control. The REPOPS-induced expression of
290 cyclin B, observed in neurons in the granule cell layer, was effectively eliminated in the
291 CyclinB-KO group (Extended Data Fig. 7b).
292 Lamin B1 expression was significantly reduced by REPOPS in both Scram-KO and
293 CyclinB-KO groups, but the degree of reduction was significantly smaller in the CyclinB-KO
294 group (Fig. 5c). Similarly, REPOPS significantly increased pH3 signals in both groups, but the
295 degree of increase was significantly reduced in the CyclinB-KO group (Fig. 5d). The
296 chromocenter ratio was significantly increased by REPOPS in the Scram-KO group, but not in
297 the CyclinB-KO group (Fig. 5e). Calbindin expression was significantly decreased in both
298 groups, but the reduction was significantly smaller in the CyclinB-KO group compared to the
299 Scram-KO group (Fig. 5f). In the open field test, REPOPS significantly increased locomotor
300 activity in the Scram-KO group from the day after the first stimulation, which remained
301 significantly greater than that of the No Stim group two weeks after the last stimulation (P =
302 0.0231, Day 24; Fig. 5g). In contrast, in the CyclinB-KO group, locomotor activity showed a
303 transient increase but gradually returned to baseline levels by Day 24 ($P > 0.99$; Fig. 5g).
304 Collectively, these findings demonstrate that cyclin B is a critical molecular mediator linking
305 repeated neuronal activation to G_2/M phase-like nuclear remodeling, neuronal immaturity, and
306 prolonged hyper-locomotor activity in mice.
307
308 **8. *ΔFosB is upregulated by Cyclin B/Cdk1 activity and mediates persistent genomic***

309 ***remodeling***

310 We next explored mechanisms underlying long-term genomic changes by
311 performing motif enrichment analysis[55] of ATAC-seq data (Fig. 1h, i). We found that open
312 chromatin peaks showed the highest similarity to ChIP-seq profiles of AP-1 transcription
313 factors, dimers composed of Fos and Jun family proteins, such as Fra1, Atf3, Batf, and JunB
314 (Extended Data Fig. 8a), suggesting that AP-1 mediates long-term genomic remodeling. We
315 focused on ΔFosB, a truncated FosB isoform, as a candidate driver of these long-term changes
316 due to its exceptionally long half-life (~208 hours[56]). We analyzed its expression time course
317 following REPOPS. After 3-day REPOPS, ΔFosB was transiently increased at 24 hours but
318 returned to baseline at 14 and 40 days (Fig. 6a). In contrast, after 10-day REPOPS, ΔFosB was
319 elevated at 24 hours and remained high at 14 and 40 days (Fig. 6a), suggesting that chronic
320 repetition of activation induces long-lasting elevation in ΔFosB. This sustained elevation likely
321 reflects increased baseline expression of Fosb rather than residual REPOPS-induced ΔFosB
322 (Fig. 6a Extended Data Fig. 8b). Notably, ΔFosB levels negatively correlated with calbindin
323 expression (Fig. 6b), which is consistent with previous reports[21], suggesting that prolonged
324 ΔFosB upregulation contributes to pseudo-immaturity of DG neurons (see also Extended Data
325 Fig. 9).

326 To examine whether cell cycle reentry is involved in this sustained ΔFosB
327 upregulation, we analyzed its expression in CyclinB-KO mice after REPOPS. At 24 hours after
328 10-day REPOPS, ΔFosB was similarly increased in both CyclinB-KO and Scram-KO groups,
329 indicating that cyclin B is dispensable for acute induction (Fig. 6c). In contrast, at two weeks,
330 ΔFosB was significantly lower in CyclinB-KO than in Scram-KO, suggesting that cyclin B
331 expression is necessary for the sustained elevation of ΔFosB. To further assess the role of
332 Cyclin B/Cdk1, we performed REPOPS while continuously perfusing its modulators—PD-
333 407824 (a Wee1 inhibitor) or BN82002 (a Cdc25c inhibitor)—via an optofluidic neural probe
334 (Extended Data Fig. 2a) and measured ΔFosB expression (Fig. 6d). Two weeks after 3-day
335 REPOPS, ΔFosB was not elevated, but PD-407824 infusion significantly increased its
336 expression (Fig. 6e). Conversely, after 10-day REPOPS, ΔFosB remained elevated for two
337 weeks, but this increase was suppressed by BN82002 (Fig. 6e). Calbindin showed a
338 complementary pattern: it remained unchanged two weeks after 3-day REPOPS but decreased
339 with PD-407824; whereas it was reduced after 10-day REPOPS but reversed by BN82002 (Fig.
340 6e). These findings indicate that Cyclin B/Cdk1 activity is essential for sustained elevation of
341 ΔFosB and the associated reduction in calbindin. Thus, repeated neuronal activation and cell
342 cycle reentry induce long-lasting and stable changes in activity-dependent transcription factors,
343 global genomic architecture, and cellular maturity.

344 **Discussion**

345 In this study, we tested the hypothesis that brain stimulation methods, such as
346 electroconvulsive therapy (ECT) and repetitive transcranial magnetic stimulation (rTMS), may
347 achieve beneficial clinical effects by reprogramming cellular state into an immature but stable
348 configuration. We developed an ECT-like optogenetic stimulation, REPetitive OPtogenetic
349 Stimulation (REPOPS), which reproducibly induces "dematuration" as indexed by global
350 changes in the cellular transcriptome and 3D genome structure. Most of these changes were
351 transient when REPOPS was repeated for three consecutive days, but could persist for more
352 than one month after 10 consecutive days of activation, consistent with the 6–12 stimulus
353 repeat regimen for ECT. RNA-seq data of human DG also showed that ECT induces immature-
354 like gene expression patterns in patients, resembling the effects by REPOPS. Underlining the
355 clinically relevant behavioral effects of REPOPS, we discovered a novel mechanism where our
356 stimulation protocol induces cell cycle re-entry resembling the G_2/M-phase-like nuclear
357 structure. These changes were reversed by deletion of Cyclin B, a master regulator of the G_2/M
358 phase transition. We further found that activation of Cyclin B/Cdk1 stabilizes ΔFosB
359 expression, thereby promoting sustained reorganization of genome structure. Our results
360 establish a candidate cellular mechanism underpinning the beneficial clinical effects of ECT
361 and offer a novel cell-based perspective for the development of brain stimulation therapies.
362

363 Our findings reveal that optogenetic stimulation of hippocampal granule cells can
364 trigger coordinated changes in gene expression, nuclear structural plasticity, and G_2/M cell
365 cycle re-entry, which collectively define an immature-like cell state. The evidence supporting
366 G_2/M cell cycle re-entry includes the increased expression of M phase-related genes such as
367 Cyclin A2, Cyclin B1, Cyclin B2, and Cdc25c, and changes in nuclear structure, including
368 nuclear lamina disruption, an increase in pH3, and chromocenter enlargement. In the literature,
369 cell cycle re-entry has been implicated in several neuropsychiatric and neurological
370 disorders[57,58]. For example, aberrant expression of cell cycle-related genes, such as Cyclin A,
371 Cyclin B, and Cdk1, has been reported in Alzheimer's disease[57,59–63] and temporal lobe
372 epilepsy[64], as well as in animal models of risk events for these diseases, such as epileptic
373 seizures[65,66], ischemia[67], and encephalitis[68]. Nuclear alterations related to the cell cycle, such
374 as nuclear lamina disruption and increased pH3, are observed in the brains of patients and
375 animal models of Alzheimer's disease[58,69,70] and epileptic seizures[71]. Recent large-scale GWAS
376 studies identified several M phase-related genes (e.g., *CCNB2, CDC25C, CENPM, CENPT,*
377 *MAD1L1,* and *STAG1*) near the risk loci for schizophrenia[72,73]. While these diseases have
378 diverse etiologies, neural hyperexcitability and cell cycle-like processes may be common

contributors to their pathophysiology[74–77]. This study is the first, to our knowledge, to show a causal link between chronic neural activation and G_2/M cell cycle re-entry. Interestingly, the cell cycle re-entry observed in various diseases is typically associated with apoptosis[78,79]; however, our REPOPS method did not induce significant cell death (Extended Data Fig. 1c). REPOPS triggered nuclear structural dynamics, but they were less pronounced than those in dividing cells during the late M phase[79,80] and there were no fully compacted chromosomes (Fig. 4e, 4g), suggesting that neurons were arrested in a G_2 to early M phase-like state for at least two weeks. Importantly, we do not assert that this immature-like cellular state is a perfect regression to developmental immaturity but rather an analog state of immaturity, a state that is phenotypically immature relative to the mature state. Another key finding of this study is the involvement of ΔFosB in neuronal dematuration. ΔFosB has previously been reported to be highly expressed in the striatum of addiction models[81,82], as well as in the DG of patients with epileptic seizures and Alzheimer's disease[21,83]. Owing to its long half-life (~208 hours)[56], ΔFosB is widely believed to mediate long-lasting cellular changes. However, given this half-life, stimulus-induced ΔFosB would be expected to decay to ~4% of its peak level within 40 days. Therefore, the marked increase observed in the Stimx10+40day group (Fig. 6a) is unlikely to reflect residual ΔFosB from prior stimulation, but rather a sustained elevation of its basal expression (Extended Data Fig. 8b). This persistent up-regulation of ΔFosB likely contributes to long-lasting 3D genome reorganization and neuronal dematuration. We also suggest that REPOPS triggers repeated calcium influx that initiates dematuration and cell cycle re-entry (Extended Data. Fig. 2a—c). Activation of calcium signalling is essential for cell cycle progression[84,85]; therefore, REPOPS-stimulated neurons may transduce a specific pattern of calcium signaling that causes cell cycle re-entry. Further studies will clarify this signaling pattern, and we predict that variations of REPOPS methodology may enable fine-scale external control of cell dematuration *in vivo*.

ECT is well documented as an effective treatment for psychiatric disorders such as severe depression and anxiety. The current results demonstrate that cellular dematuration triggered by an ECT-like stimulus can produce positive behavioral phenotypes, including decreased depression-like symptoms and increased motor activity, similar to the clinical ECT effects. An important question is how these behaviors are enabled by neuronal stimulation at the neural circuit level. REPOPS increased the number of speed cells and the speed coding accuracy in the DG (Fig. 3i–k). Prior studies indicate that activation of DG neurons can elicit robust exploration of the environment[48], and our observation of increased speed-related activity in the DG may account for the increased locomotor activity observed in the open field (Fig. 2a,

414 2b) and home cage (Fig. 2c). Activation of DG neurons is also known to suppress depression-
415 like behaviors[86,87], therefore, increased speed-related activities of DG neurons may explain the
416 link between ECT-like stimulation and the reduction in depression-like behavior observed in
417 the tail suspension and forced swim tests (Fig. 2d, 2e). In contrast to these beneficial effects, a
418 potential negative side effect of ECT is memory loss, including retrograde and anterograde
419 amnesia[88,89]. Indeed, we observed a deficit in remote memory, or the ability to recall
420 information from neocortex into the hippocampal circuit (Extended Data Fig. 3a and
421 Supplementary results 2). REPOPS caused long-term (> 2 weeks) alterations in synapse-related
422 genes, including *Gria1*, *Gria2*, *Camk2a*, *Camk2b*, and *Arc* (Fig. 1e). Reanalysis of RNA-seq
423 data from human patients with and without ECT also revealed significant changes in the
424 expression of *GRIA1, GRIA2,* and *ARC* (Fig. 1g). These genes play pivotal roles in synaptic
425 and homeostatic plasticity[90–92] and their decline may be related to memory impairment due to
426 neural hyperexcitation. Long-term down-regulation in the expression of synapse-related genes
427 may interfere with the development of place cells and spatial information coding in the DG
428 (Fig. 3f–h) and CA1[16,93–95]. Such REPOPS-dependent deficit in neural plasticity may share a
429 common mechanism with ECT-induced amnesia. Thus, ECT-like REPOPS alters neural coding,
430 leading to both decreased depressive-like behaviors and memory deficits. Further research will
431 address the ECT stimulus conditions that do not impair memory and learning, but preserve
432 beneficial clinical therapeutic effects.
433
434 Our findings also provide a novel perspective on the mechanism of action of
435 antidepressant therapy. In this study, we found that REPOPS-triggered cellular and behavioral
436 effects share intriguing similarities to previously reported behavioral effects and neuronal
437 dematuration induced by ECS or selective serotonin reuptake inhibitors (SSRIs)[9,10,39,40].
438 Chronic SSRI treatment may reactivate the plastic state in the adult brain, comparable to that
439 observed during development[14,41]. For example, in the adult visual cortex, chronic fluoxetine
440 reopens a critical period of plasticity for the recovery of visual function[96,97], and, in the
441 hippocampus, increased neural circuit plasticity can promote fear memory extinction[14,98].
442 SSRIs may regulate neural plasticity by increasing the environmental susceptibility of neural
443 circuits, thereby reducing depression via exposure to favorable environments[99,100]. This form
444 of "meta-plasticity"[101,102], or the induction of changes in neural plasticity itself, can also
445 manifest in opposite forms by neural hyperactivity. A recent study showed that recurrent
446 seizures cause a long-term reduction in neuronal excitability, indicating decreased neural
447 plasticity[103]. In the current study, REPOPS for 10 days inhibited spatial map formation by
448 exposure to the environment for more than two weeks (Fig. 3f–h), suggesting an altered meta-

plasticity for spatial coding. Thus, neural overactivation and dematuration can alter the meta-plasticity of neural circuits, which may underlie the effects of antidepressant treatments such as ECT and rTMS, or the development of neuropsychiatric disorders involving neural hyperexcitability in their etiology. A key insight from the present work is that the immature cellular state appears to be bistable; that is, it can serve as a reversible therapeutic intermediate, as observed in ECT, or consolidate into an irreversible pathological lesion, as seen in disease models.

In summary, we propose a working model for the mechanism of brain stimulation therapies in the treatment of psychiatric disorders. This class of brain diseases may represent neuronal populations trapped in various energy minima of metabolic and/or synaptic inflexibility, such as the loss of plasticity by the pathological closure of neural circuits to environmental stimulation, as discussed above. In this model, repetitive brain stimulation methods like ECT or rTMS trigger patterned calcium influx and signaling to drive cellular dematuration that temporarily resets cellular metabolic and synaptic homeostasis to restore normal neural circuit flexibility and beneficial clinical outcomes like anti-depressive behavior. This immature-like state can persist for more than one month, and excessive neuronal activation may eventually reinforce rather that reset metabolic or synaptic dysfunction in a vicious cycle associated with chronic psychiatric disorders associated with hyperactivity. Therefore, our model suggests that the immature-like cell state may serve as a bistable switch for cellular health at moderate levels of electrical brain stimulation, or disease progression at higher levels. We believe that these findings open a window to novel methods and protocols for artificial neural stimulation that may enable cell reprogramming for brain health.

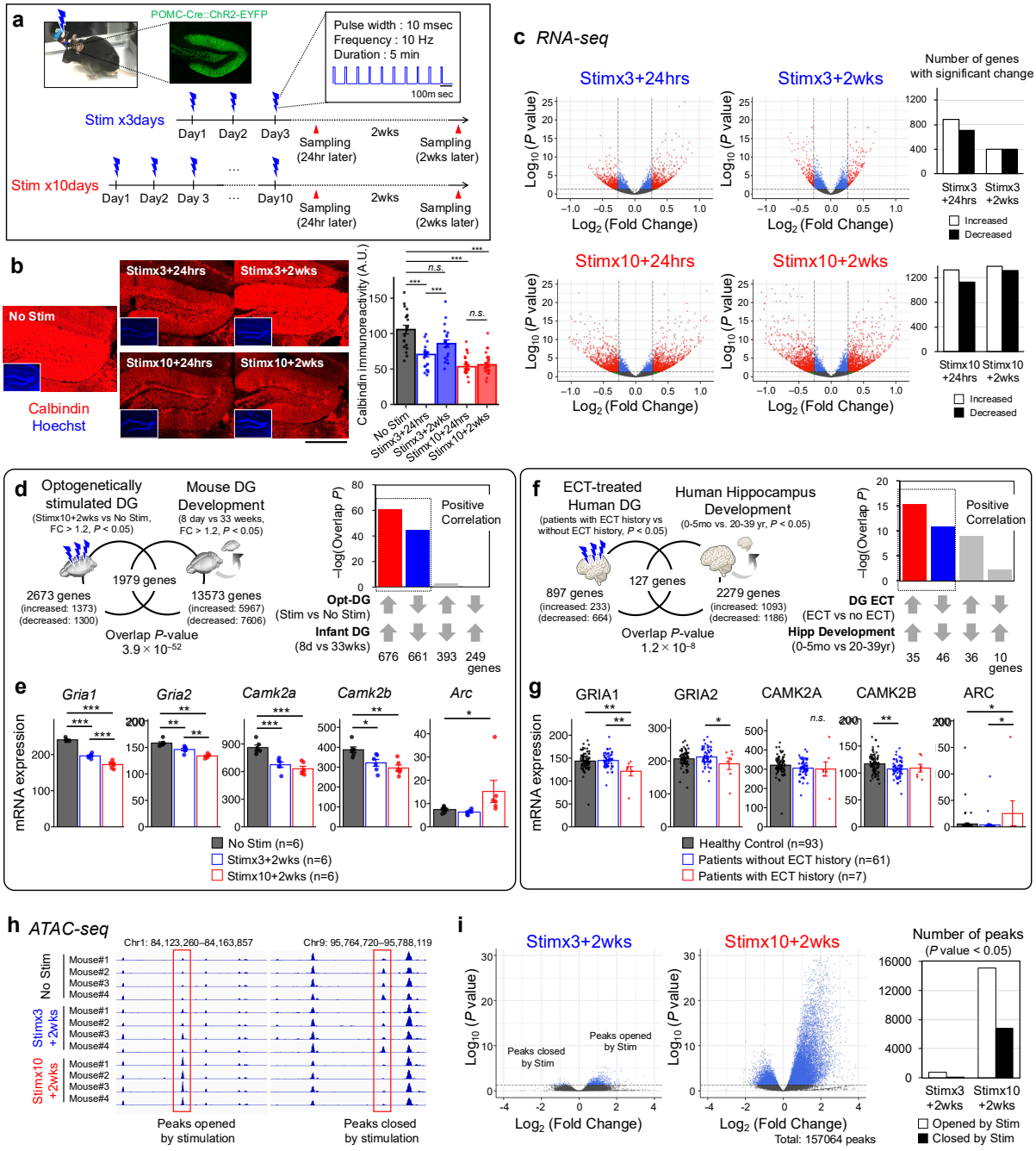

Figure 1. REPOPS induces long-term changes in gene expression, chromatin accessibility, and locomotor activity in mice

a, Experimental design. POMC-Cre::ChR2-EYFP mice express ChR2 in GCs of the DG. Blue light was delivered via a wireless LED device. Optogenetic stimulation (10-msec pulse at 10 Hz for 5 min/day) was applied for 3 or 10 consecutive days. Brains were collected 24 hours or two weeks after the last stimulation.

b, Immunohistostaining of calbindin, a maturation marker of GCs, in dorsal DG. Scale bar, 500 μm. Bar graph shows calbindin immunoreactivity (10–15 sections from 4 mice in each group).

Error bars represent the Mean ± s.e.m. One-way ANOVA followed by Bonferroni correction for multiple comparisons, $F_{(4,106)} = 24.9$, $P = 1.5 \times 10^{-14}$, ***$P < 0.001$.

c, RNA-Seq. Volcano plots show fold change and *P* values distribution after differential transcript abundance analysis using DESeq2. All stimulation groups were compared with the No Stim group (n = 6 mice per group). Genes with significantly differential expression ($P < 0.05$; fold change > 1.2) are highlighted in red. Bar graphs indicate number of genes with significant changes (i.e. red dots in Volcano plots).

d, Overlap between genes altered by REPOPS (Stim×10+2wks vs. No Stim) and during normal development of the mouse DG (P8 infants vs. 33-week-old adults; GSE113727). Bar graphs show–$\log_{10}$ of overlap *P*-values for genes upregulated or downregulated by each condition. The Bonferroni correction was used to adjust the significance level according to the number of dataset pairs.

e, mRNA expression levels (FPKM) of representative synapse-related genes. Mean ± s.e.m. (n = 6 mice/group). One-way ANOVA followed by Bonferroni correction for multiple comparisons; *$P < 0.05$, **$P < 0.01$, ***$P < 0.001$.

f, Overlap between genes altered in DG of human patients with bipolar disorder and major depressive disorder (with a history of ECT vs. without ECT; SRP241159[45]) and those altered during human hippocampal development (0-5 month infants vs. 20-39-year-old adults; GSE25219[46]).

g, mRNA expression levels (FPKM) of representative synapse-related genes in post-mortem DG from healthy control subject (n=93), patients without ECT history (n=61), and patients with ECT history (n=7).

i ATAC-seq. Integrative Genomics Viewer (IGV) visualization of representative gained-open and gained-closed chromatin profiling coverage.

j, Volcano plot showing the fold change and *P* value distribution after differential analysis of chromatin accessibility using DESeq2. Stim×3+2wks and Stim×10+2wks groups were compared with the No Stim group (n = 4 mice/group). Bar graph shows number of peaks with a significant change ($P < 0.05$).

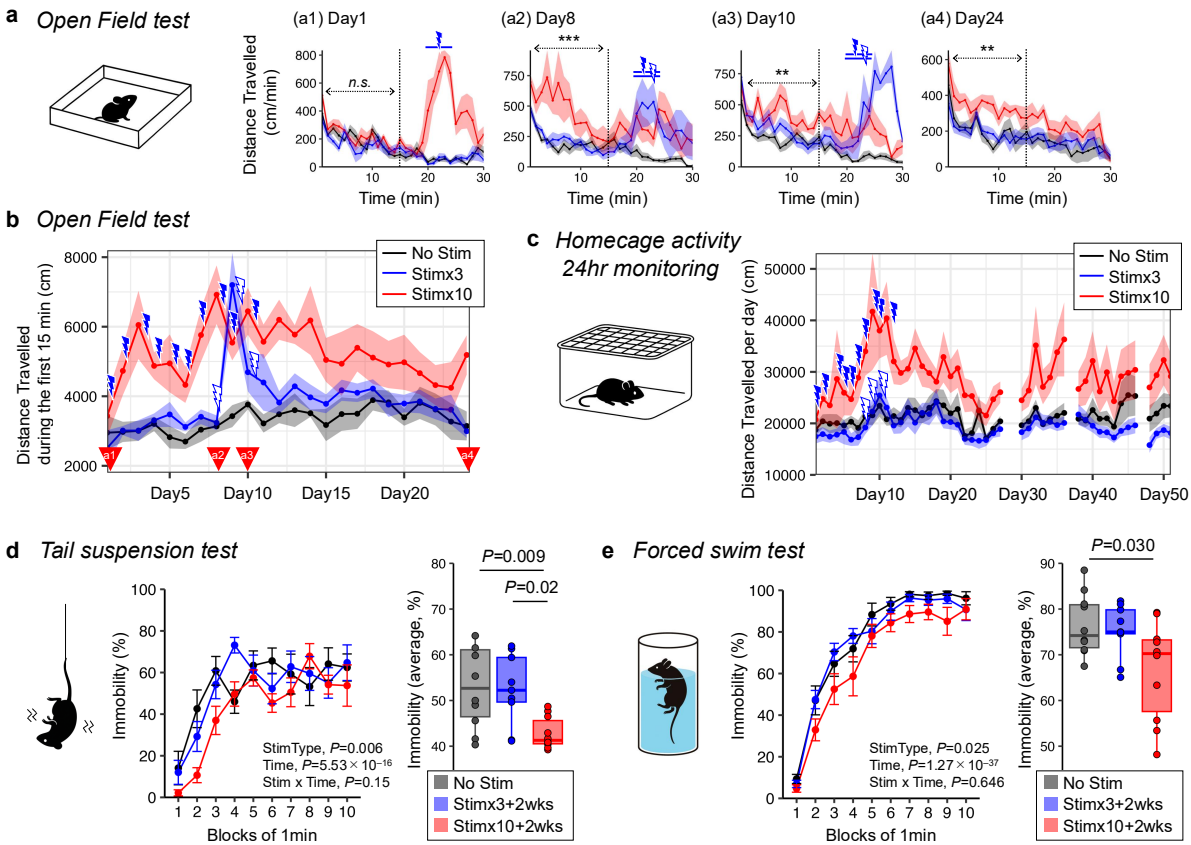

Figure 2. REPOPS induces anti-depressive behaviors

a, Distance traveled in the open field during the first 30 min on Day 1 (a1), Day 8 (a2), Day 10 (a3), and Day 24 (a4), corresponding to time points in **b** (red arrowheads). Solid lines show group means (n = 6 mice/group); semitransparent area indicates ± s.e.m. (black, No Stim; blue, Stim×3+2wks; red, Stim×10+2wks). Optogenetic stimulation was introduced for 5 min (20–25 min after the start) on Day 1, Day 8, and Day 10. Asterisk indicates Stim×10+2wks vs. No Stim; One-way ANOVA with Bonferroni correction; $*P < 0.05$, $**P < 0.01$, $***P < 0.001$.

b, Total distance traveled in the first 15 min of the open field test from Day 1 to Day 24. Two-

way repeated measures ANOVA; Stim type, $F_{(2, 14)} = 9.96$, $P = 2.0\times10^{-3}$; Day, $F_{(23, 322)} = 5.08$, $P = 4.63\times10^{-12}$. Stim type × Day, $F_{(46, 322)} = 2.58$, $P = 7.81\times10^{-7}$.

c, 24-hour locomotor activity in the home cage. Daily average distance traveled is shown (n = 10, 8, and 10 mice for No Stim, Stim×3, and Stim×10 groups, respectively). Data missing on Day 28, 29, 37 and 47 due to computer system error. $P < 0.05$ on Day 7–8, 10–16, 20, 22–23, 25–30, 33–36 (Stim×10 vs. No Stim).

d, Immobility (%) in tail suspension test. Values are the Mean ± s.e.m. Two-way repeated-measures ANOVA results shown in panel. n = 10, 9, and 10 mice. Box plot summarizes average immobility over 10 min. One-way ANOVA with Bonferroni correction; $^{*}P < 0.05$, $^{**}P < 0.01$, $^{***}P < 0.001$.

e, Same as **d**, for immobility (%) in the forced swim test.

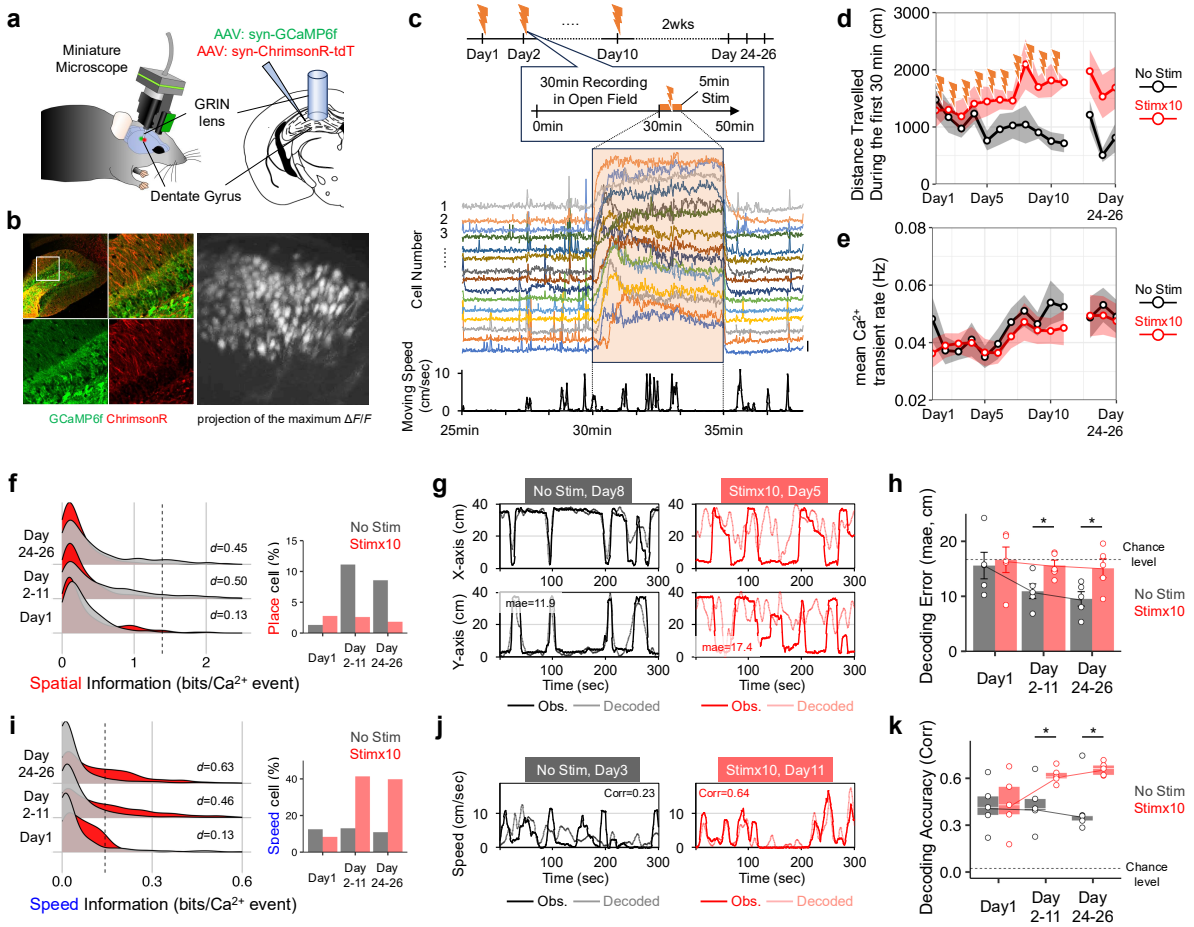

Figure 3. REPOPS mediates long-term changes in neural coding of navigational information

a, Simultaneous *in vivo* calcium imaging and optogenetic stimulation under free-moving conditions. AAV-syn-GCaMP6f and AAV-syn-ChrimsonR were co-injected into the DG, followed by GRIN-lens implantation. An integrated miniature microscope (nVoke; Inscopix) enabled large-scale cellular-resolution Ca^{2+} imaging and optogenetic stimulation.

b, Left: Expression of GCaMP6f and ChrimsonR in the DG. Right: Max projection of relative fluorescence change ($\Delta F/F$) of Ca^{2+} transients from all imaging frames during the first 30 min,

showing representative active neurons.

c, Top: Experimental design of Ca^{2+} imaging combined with optogenetic stimulation during the open field test. Each 50-min session consisted of 30-min Ca^{2+} imaging (used for the following analysis), 5-min optogenetic stimulation, and 15-min post-stimulation recording. This was repeated for 10 days. No light was introduced to mice in the No Stim group. Bottom: $\Delta F/F$ traces from 15 representative neurons (scale bar, 10% $\Delta F/F$). Data from 25 to 38 min of a 50-min session are shown.

d, Distance traveled during the first 30 min

e, Average Ca^{2+} transient rate during the first 30 min.

f, Distribution of spatial information for the No Stim (grey curve) and Stim×10 groups (red curve). The vertical axis represents the frequency of distribution, with the dotted line indicating the criterion for place cells (top 95% percentile of the shuffled distribution; see Methods section). Bar graph indicates proportion of place cells.

g, Representative results of position decoding using Ca^{2+} imaging data. The first 30 min was split into two 15-min halves for training and test data for decoding. Black/red lines: observed position; grey/pink lines: decoded position.

h, Decoding accuracy (mae; mean absolute error, cm). Dotted lines: shuffled control. Two-way repeated measures ANOVA: Stim type, $F_{(1, 8)} = 6.49$, $P = 0.034$; Day, $F_{(2, 16)} = 2.89$, $P = 0.085$; Stim type × Day, $F_{(2, 16)} = 1.11$, $P = 0.353$. Bonferroni correction for multiple comparisons was performed, $^*P < 0.05$.

i, Same as **f**, but for speed information and speed cells. The dotted line indicates the criterion for speed cells (top 99% percentile of the shuffled distribution).

j, Same as **g**, but for speed decoding.

k, Same as **h**, but for speed decoding accuracy. Two-way repeated measures ANOVA: Stim type, $F_{(1, 8)}=4.02$, $P = 0.080$; Day, $F_{(2, 16)} = 4.87$, $P = 0.022$; Day×Stim type, $F_{(2, 16)} = 3.98$, $P = 0.039$. Bonferroni correction for multiple comparisons was performed, $^*P < 0.05$.

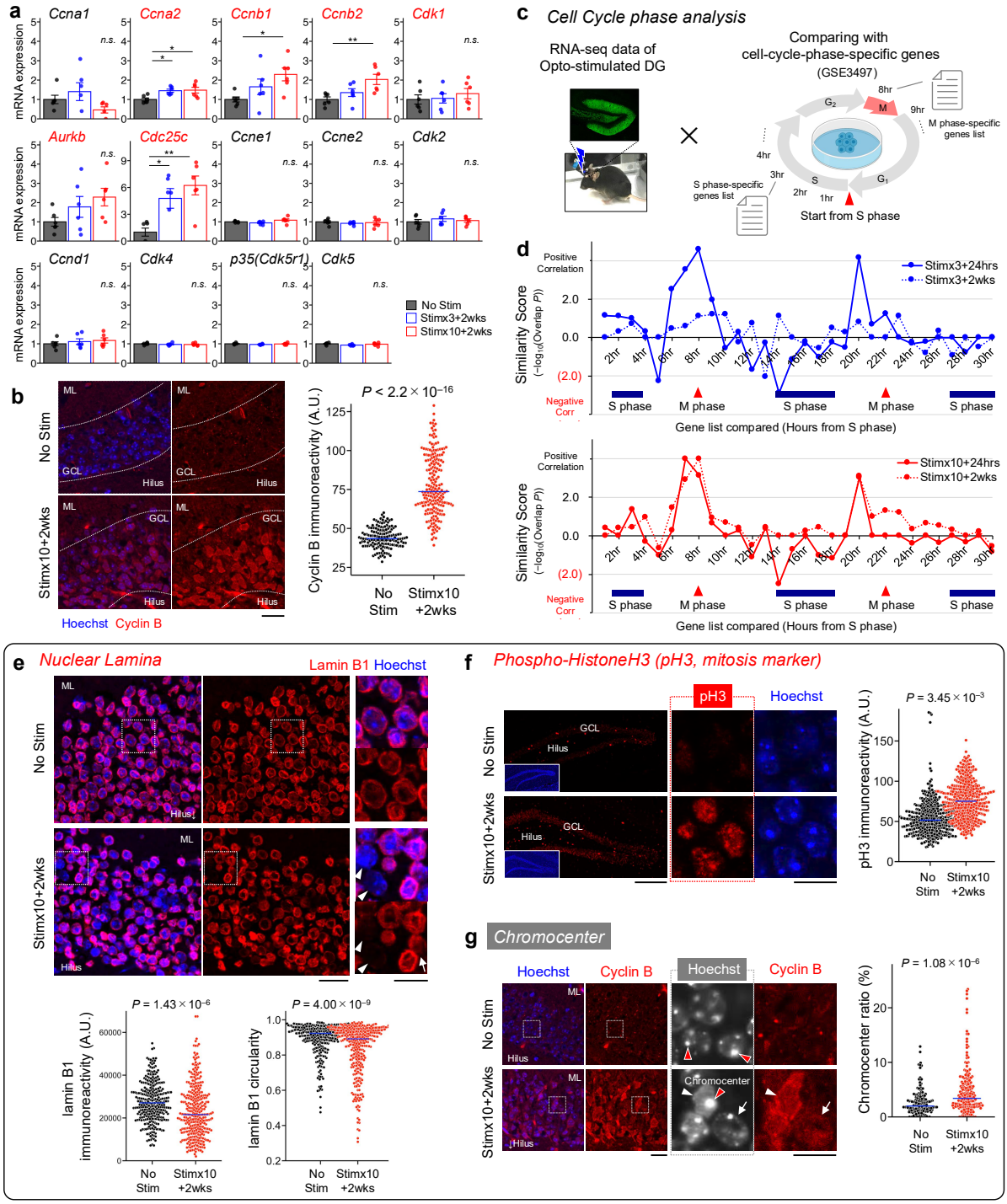

Figure 4. REPOPS confers G_2/M phase-like gene expression patterns and nuclear structure plasticity

a, Expression of representative cell cycle-related genes. mRNA expression levels (FPKM) are normalized to the control group (No Stim). Data are shown as mean ± s.e.m. (n = 6 mice/group). One-way ANOVA with Bonferroni correction; *$P < 0.05$, **$P < 0.01$.

b, Cyclin B immunostaining (red) in the DG. Beeswarm plot shows cyclin B immunoreactivity

579 in individual neurons. Blue bars indicate the median values of 147 neurons (No Stim) and 202
580 (Stim×10+2wks) neurons from three biologically independent samples. ML, molecular layer;
581 GCL, granule cell layer.
582 **c,** Cell cycle phase analysis. To infer the cell cycle-like status of DG neurons after REPOPS,
583 RNA-seq data from optogenetically stimulated DG (Fig. 1c) were compared with publicly
584 available reference gene expression profiles representing each phase of the cell cycle. These
585 reference profiles were derived from microarray data of HeLa cell sampled at 1-hour intervals
586 (1-30 h) after release from S phase arrest (Whitfield *et al.*, 2002; GSE3497)[50].
587 **d,** Similarity in gene expression patterns between optogenetically stimulated DG and gene
588 expression profiles representing each phase of the cell cycle. Similarity scores were calculated
589 as –log of the overlap *P* value between RNA-seq data of stimulated DG and gene sets
590 representing each time point of the cell cycle (1–30 hours from the start of S phase). Positive
591 scores indicate concordant expression changes (e.g., both upregulated), while negative scores
592 indicate opposite trends. The positions of the S and M phases on the x-axis reflect cell cycle
593 timing estimated from the HeLa cell data (GSE3497; Whitfield et al., 2002)[50].
594 **e,** Lamin B1 immunostaining (red) in the DG. Enlarged views of boxed regions are shown at
595 right. Arrows and arrowheads indicate neurons with partial or complete disruption of lamin B1
596 structure. Scale bars: 20 μm (left), 10 μm (right). Beeswarm plots show immunoreactivity and
597 circularity of lamin B1 in individual neuron (n = 289 and 320 neurons from three independent
598 samples). Blue bars, medians. Welch's *t*-tests: immunoreactivity, $t_{(589)} = 4.87$, $P = 1.45 \times 10^{-6}$;
599 circularity, $t_{(547)} = 5.87$, $P = 7.38 \times 10^{-9}$.
600 **f,** Immunostaining of phospho-histone H3 (pH3) (red) in the DG. Scale bars: 200 μm (left), 10
601 μm (right). Beeswarm plot shows pH3 signal intensity in individual neurons (n = 415 and 459
602 neurons from three independent samples). Welch's *t*-test: $t_{(858)} = 14.1$, $P < 2.2 \times 10^{-16}$.
603 **g,** DNA counterstaining with Hoechst (blue and white pseudo-color) and cyclin B
604 immunostaining (red) in the DG. Enlarged views of boxed areas are shown on the right. Red
605 arrowheads indicate chromocenters–an aggregation of the heterochromatin domain visible by
606 Hoechst staining. White arrowheads/arrows: neurons with large/small chromocenters and
607 high/low cyclin B expression, respectively. Scale bars: 100 μm (left), 10 μm (right). Beeswarm
608 plot shows the chromocenter ratio (%) per neurons (n = 147 and 202 neurons from three
609 independent samples). Welch's *t*-test: $t_{(306)} = 5.46$, $P = 9.38 \times 10^{-8}$.
610

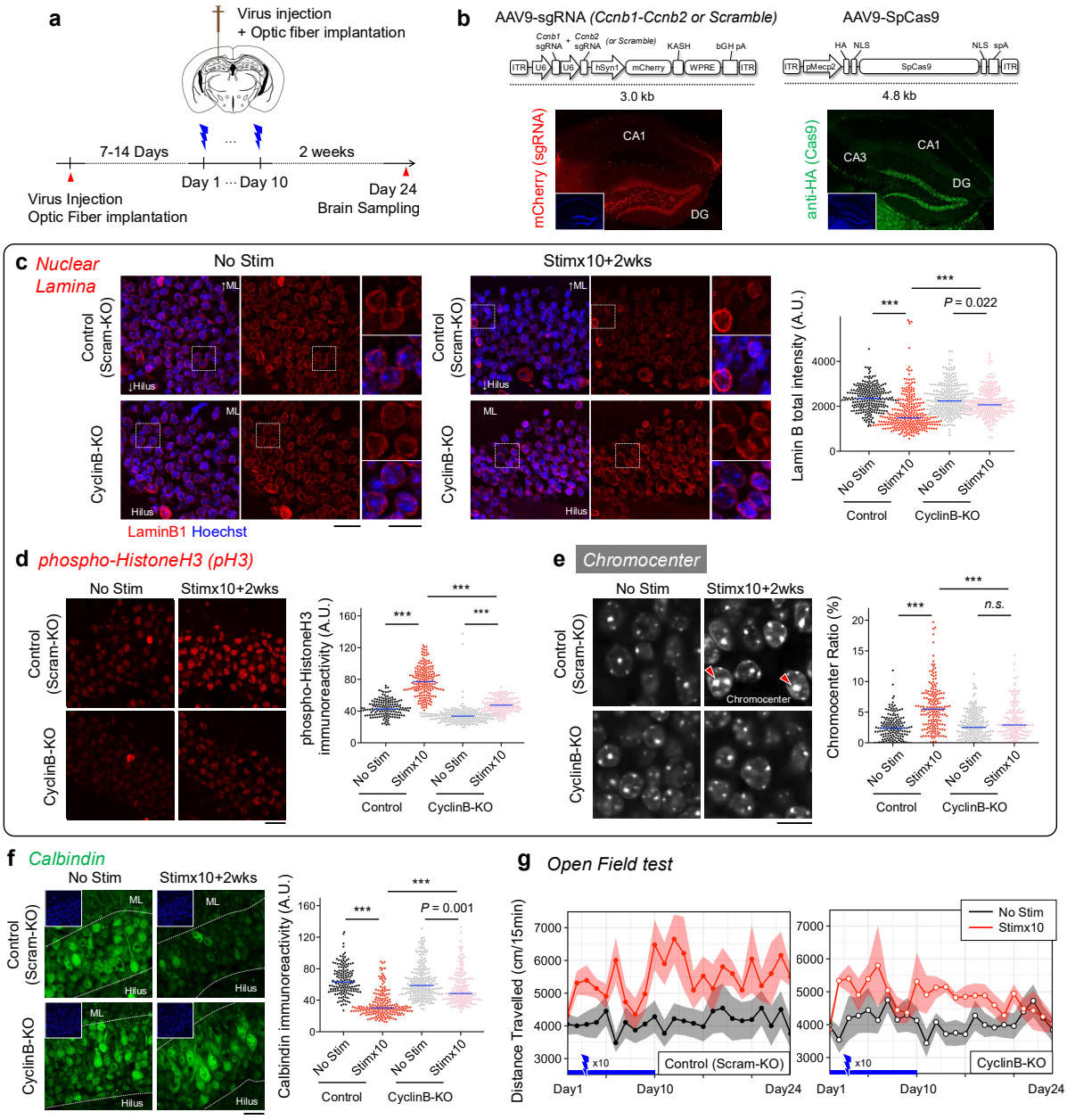

611

612 ***Figure 5. Cyclin B deletion reverses multiple REPOPS-induced phenotypes***

613

614 **a,** Experimental design. AAV9 vectors encoding Cas9 and sgRNAs targeting *Ccnb1* and *Ccnb2*
615 (CyclinB-KO) or a *Scramble* sequence (Scram-KO) were co-injected into the DG, followed by
616 optic fiber implantation. After 7-14 days, optogenetic stimulation was performed for 10
617 consecutive days. Brains were sampled 2 weeks after the last stimulation. The open field test
618 was conducted from Day 1 (immediately before the first stimulation) to Day 24 (two weeks
619 after the last stimulation).

620 **b,** Co-expression of sgRNAs and Cas9 in the DG. sgRNAs were co-expressed with mCherry,
621 and Cas9 was tagged with HA. Most neurons in the granule cell layer showed both mCherry
622 and HA immunoreactivity.

c, Lamin B1 immunostaining in the DG (converted to red for visibility; originally stained with Alexa647). Upper and lower panels show control (Scramble-KO) and *Ccnb1*-*Ccnb2*-KO (CyclinB-KO) mice, respectively. Scale bars: 20 μm (left), 10 μm (right). Beeswarm plot shows lamin B1 immunoreactivity. Red bars, median. One-way ANOVA, $F_{(3, 679)} = 60.19$, $P < 2.0 \times 10^{-16}$; Bonferroni corrected, ***$P < 0.001$. n = 245, 301, 271, and 246 neurons from three independent samples per group.

d, pH3 immunostaining in the DG. One-way ANOVA, $F_{(3, 679)} = 325.7$, $P < 2.0 \times 10^{-16}$; ***$P < 0.001$; 199, 158, 143, and 183 neurons from five independent samples per group. Scale bar, 20 μm.

e, Chromocenter visualized by Hoechst staining (white, pseudo-color). One-way ANOVA, $F_{(3, 679)} = 39.1$, $P < 2.0 \times 10^{-16}$; ***$P < 0.001$; 199, 158, 143, and 183 neurons from five independent samples per group. Scale bar, 10 μm.

f, Calbindin staining in the DG. One-way ANOVA, $F_{(3, 725)} = 104.3$, $P < 2.0 \times 10^{-16}$; ***$P < 0.001$; 217, 157, 162, and 198 neurons from five biologically independent samples per group. Scale bar, 20 μm.

g, Open field test: total distance traveled during the first 15 min from Day 1 to Day 24. Left: Scramble-KO; Right: CyclinB-KO. Black and red lines represent No Stim and Stim×10+2wks groups, respectively. Solid lines, group means (n = 7 mice/group); semitransparent areas, ±s.e.m. Two-way repeated measures ANOVA: Groups, $F_{(3, 24)} = 4.271$, $P = 0.015$; Day, $F_{(6, 163)} = 4.271$, $P = 0.0204$; Groups×Day, $F_{(20, 163)} = 1.09$, $P = 0.36$.

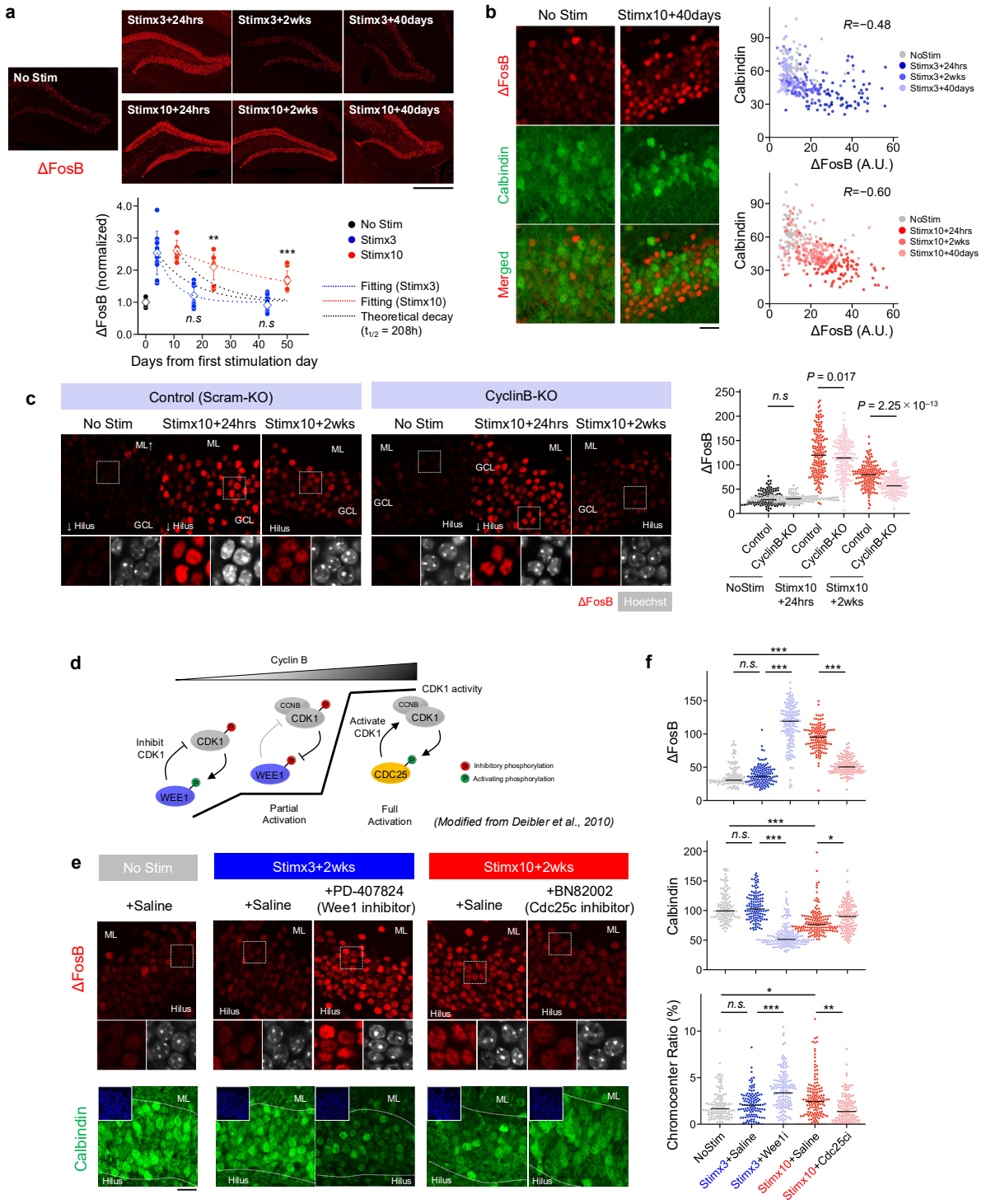

644

645 ***Figure 6. Cyclin B/Cdk1 activity mediates long-term ΔFosB expression and pseudo-***
646 ***immaturity of neurons***

647

648 **a,** Top, ΔFosB immunostaining in the DG. Scale bar, 500 μm. Bottom, time course of ΔFosB
649 expression. Day 0 denotes the first stimulation day. Values were normalized to the mean of the
650 No Stim group. The black dashed line indicates the theoretical decay of ΔFosB (half-life = 208
651 h); blue and red curves represent exponential fits for the Stim×3 and Stim×10 groups,

respectively. n = 9–11 slices per group. One-sample *t*-tests were performed between observed values and the theoretical decay curve; ***$P < 0.001$.

b, Immunostaining of ΔFosB and calbindin in the DG (same data as in panel a). Only No Stim and Stim×10+40 days are shown. Scale bar, 20 μm. Right, scatter plot showing the correlation between ΔFosB and calbindin immunoreactivity.

c, ΔFosB immunostaining in the DG of Scram-KO and CyclinB-KO mice (same mice as in Fig. 5). Bottom panels show enlarged views of the white boxes. Grayscale indicates Hoechst staining. Scale bar, 20 μm. Beeswarm showing ΔFosB immunoreactivity (n = 129–165 cells per group). Black bars indicate the median. One-way ANOVA: $F_{(5, 859)} = 270.94$, $P < 2.0 \times 10^{-16}$; post hoc comparisons with Tukey's test.

d, Schematic of Cyclin B/Cdk1 activation (modified from Deibler *et al.* 2010[104]). Cdk1 is activated as cyclin B accumulates. This activation is inhibited by Wee1 and promoted by Cdc25c.

e, Top, ΔFosB immunostaining in the DG. Middle, enlarged view of the boxed region. Grayscale indicates Hoechst staining. Bottom, calbindin immunostaining. Scale bar, 20 μm.

f, Beeswarm plots showing ΔFosB, calbindin, and chromocenter ratio. n = 114–156 cells per group. Black bars indicate the median. One-way ANOVA: ΔFosB: $F_{(4, 649)} = 405.45$, $P < 2.0 \times 10^{-16}$; Calbindin: $F_{(4, 655)} = 117.65$, $P < 2.0 \times 10^{-16}$; Chromocenter ratio: $F_{(4, 655)} = 14.63$, $P < 2.0 \times 10^{-16}$. Multiple comparisons were corrected using Tukey's test.

672 **Materials and Methods**

673

674 ***Animals***

675 *ROSA26-CAG-stop^{flox}-ChR2(H134R)-EYFP* (Strain#012569; RRID:IMSR_JAX:012569) and
676 *POMC-Cre* (Strain #010714; RRID:IMSR_JAX:010714) were obtained from Jackson
677 Laboratories (Bar Harbor, Maine). These mouse lines were crossed to generate POMC-
678 Cre::ChR2-EYFP mice, which express ChR2-EYFP selectively in the granule cells (GCs) of
679 the dentate gyrus (DG) (Fig. 1a). Mice were used for experiments at 3–4 months of age for
680 RNA-seq and ATAC-seq experiments, and at 6–12 months for other experiments. Three or four
681 mice were housed in one cage and switched to individual housing 1–2 weeks prior to the
682 experiment. They were housed with a 12 hr light/dark cycle (lights on at 7:00 a.m., off at 7:00
683 p.m.) with access to food and water *ad libitum*. The room temperature was maintained at 23 ±
684 2°C. All the experiments were conducted during the light period. All animal experiments were
685 approved by the Institutional Animal Care and Use Committee of Fujita Health University
686 based on the Law for the Human Treatment and Management of Animals and the Standards
687 Relating to the Care and Management of Laboratory Animals and Relief of Pain. Every effort
688 was made to minimize the number of animals used.

689

690

691

692 ***Stereotactic Surgery***

693

694 *Optic fiber implantation*

695 For optogenetic stimulation, a blue-light optic fiber was implanted into the dorsal DG of adult
696 POMC-Cre::ChR2-EYFP mice using conventional methods[105]. Briefly, adult mice were
697 anesthetized with 1.5–3% isoflurane at an oxygen flow rate of 1 L/min. The head fur was
698 shaved and the incision site was sterilized with 70% ethanol before the surgical procedure. The
699 mice were mounted on a stereotaxic device (Narishige, Tokyo, Japan). After the scalp was
700 incised and pulled aside, a 1.0 mm diameter craniotomy was created with a surgical drill on
701 the skull above the implantation site. Using the stereotaxic device, a 250 μm diameter optic
702 fiber (470 nm, fiber diameter 250 μm; TeleC-B-3mm-250μm, Bioresearch Center, Aichi,
703 Japan) was precisely inserted into the target site (2.0 mm posterior to bregma (AP), 1.5 mm
704 lateral to midline (ML), and 1.5 mm ventral to bregma (DV)) and fixed to the skull with dental
705 cement. After implantation, the scalp was sutured and treated with povidone-iodine. To avoid
706 the effects of surgery on mouse behavior, a recovery period of 5–10 days after surgery was

707 provided when performing behavioral experiments.
708
709 *Stereotactic injection of AAV9*
710 For the genome editing experiment (Fig. 5), a mixture of adeno-associated virus (AAV)
711 carrying Cas9 and sgRNA was injected into the DG immediately before optic fiber
712 implantation. For dominant-negative inhibition of ΔFosB experiment (Extended Data Fig. 9),
713 we injected an AAV expressing ΔJunD (a kind gift from A.J. Robison) was injected.
714 Anesthetization and craniotomy were performed in the same way as described above. A glass-
715 capillary pipette (25 μm inner-diameter tip) filled with the virus suspended in mineral oil was
716 inserted into the target site (2.0 mm posterior to bregma (AP), 1.5 mm lateral to midline (ML))
717 through the surgical drill on the skull. A 200 nL of 1:3 AAV mixture of AAV9-U6-sgRNA
718 (*Ccnb1-Ccnb2* or Scramble)-hSyn1-mCherry (2.0×10^{13} vector genomes vg/ml) and AAV9-
719 pMecp2-HA-SpCas9 (2.0×10^{13} vg/ml) was injected at 200 nL/min using a microinjection
720 pump (Nanoliter 2010, WPI, FL) at three depths (1.5 mm, 2.0 mm, and 2.5 mm). After each
721 injection, a glass pipette was held in place for 1–2 min before retraction to prevent leakage.
722 Shortly after virus injection, the optic fiber was embedded in the same site using the procedure
723 described above.
724
725 *Implantation of injection cannula*
726 In the experiment that combined optogenetic stimulation and drug injection (Fig. 6d–f and
727 Extended Data Fig. 2), a guide cannula (24-gauge, 11 mm length, C316G, Plastics One) was
728 implanted into the dorsal DG using the same procedure as that used for optic fiber implantation.
729
730
731
732 ***Optogenetic Stimulation and drug infusion***
733 For optogenetic stimulation under freely moving conditions, we employed a wireless LED
734 illuminator, Teleopto (BioResearch Center, Nagoya, Japan). A 2.0g infrared receiver (TeleR-2-
735 P, BioResearch Center) was attached to an optic fiber implanted in the mouse head, whereas in
736 the control group, a dummy receiver was used as a substitute. This receiver was signalled by
737 an infrared generator (TeleEmitter-C, BioResearch Center) to light up the optic fiber. The light
738 intensity varied depending on the custom-made fiber, typically within a range of 3–5 mW. We
739 set the stimulation protocol to 10 msec pulses at a frequency of 10 Hz, utilizing a pulse
740 generator (STOmk-2, BioResearch Center). These photostimulation intensities are sufficiently
741 weak to avoid tissue damage[106].

742 For optogenetic stimulation with an intracerebral drug infusion (Fig. 6d–f and Extended Data
743 Fig. 2), we employed injection cannulas (31-gauge, 11 mm length, C316I, Plastics One) and
744 customized optic fibers designed to fit the implanted guide cannula (Bio Research Center). For
745 acute injection (Extended Data Fig. 2), the injection cannula was attached to the implanted
746 guide cannula, and 2uL of the drugs was injected over approximately 5 min. The Ca^{2+} blockers
747 consisted of 100 mM NBQX (ab120046, Abcam), 100 mM AP5 (ab120003, Abcam), 100 mM
748 mibefradil (ab120343, Abcam), and 100 mM nimodipine (ab120138, Abcam) diluted in saline
749 (Extended Data Fig. 2c). Kinase inhibitors, K252a (sc-200517, Santa Cruz), SB218078 (sc-
750 203692, Santa Cruz), Dasatinib (sc-218081, Santa Cruz), and Ro-32-0432 (sc-3549, Santa
751 Cruz), were used at the same concentration (1.0 mM). Five minutes after the injection, the
752 injection cannula was gently detached, and a customized optic fiber was inserted through the
753 guide cannula. For chronic drug infusion (Fig. 6d–f), an osmotic pump (Alzet model 1004) was
754 implanted subcutaneously and connected to a guide cannula. The pump was filled with PD-
755 407824 (sc-203669, Santa Cruz) or BN82002 (#217691, Calbiochem) and delivered the drug
756 at a constant rate. For the effective infusion of drugs into brain tissues *in vivo*, the concentration
757 of the solution was set to 100–1000 times higher than that used for bath applications in acute
758 slice cultures according to previous studies[107]. Stimulation was performed in the same manner
759 as described above. All procedures were conducted in an awake state.
760
761
762
763 ***RNA-Sequencing Library Construction, Sequencing, Mapping, and Data Analysis***
764 The dentate gyrus was rapidly dissected from the adult mouse hippocampus under a dissection
765 microscope as previously described[108]. Previous studies have shown that such preparations are
766 highly enriched with mature dentate granule neurons (–90% $NeuN^{+}$ neurons[30,109]; see also
767 Extended Data Fig. 7a). Total RNA from dissected tissue samples was extracted using
768 NucleoSpin RNA (Macherey-Nagel, Duren, Germany), according to the manufacturer's
769 instructions. The RNA quality was assessed with an Agilent 2200 TapeStation (Agilent
770 Technologies, Santa Clara, CA, United States). Sequencing libraries were prepared using the
771 TruSeq Stranded mRNA Sample Prep Kit (Illumina, San Diego, CA, USA) and sequenced as
772 100-bp paired-end reads on the Illumina HiSeq 2500. Sequenced data were mapped onto the
773 Mus musculus genome (GRCm38/mm10) using TopHat (v2.0.14). Fragments per kilobase per
774 million (FPKM) values were computed by Genedata Profiler Genome (v10.1.12). Genes with
775 low expression (FPKM < 0.1) were excluded from the analysis to avoid an excessively high
776 FDR due to low expression levels.

ATAC-Sequencing Library Construction, Sequencing, Mapping, and Data Analysis

The dentate gyrus of adult mice was dissected in the same manner as that used for RNA-seq. The dentate gyrus was slowly frozen in a freezing box (Cat. No. 5100-0001; Mr. Frosty Freezing Container, Thermo Fisher Scientific). Flash-frozen tissue was sent to Active Motif to perform the ATAC-seq assay. The tissue was manually dissociated, isolated nuclei were quantified using a hemocytometer, and 100,000 nuclei were tagmented as previously described[110], with some modifications based on Corces et al. 2017[111] using the enzyme and buffer provided in the Nextera Library Prep Kit (Illumina). Tagmented DNA was purified using the MinElute PCR purification kit (Qiagen), amplified with 10 cycles of PCR, and purified using Agencourt AMPure SPRI beads (Beckman Coulter). The resulting material was quantified using the KAPA Library Quantification Kit for Illumina platforms (KAPA Biosystems) and sequenced using PE42 sequencing on a NextSeq 500 sequencer (Illumina). For the analysis of ATAC-seq data, we first aligned reads using the BWA algorithm (mem mode; default settings). Duplicate reads were removed, and only reads mapping as matched pairs and uniquely mapped reads (mapping quality >= 1) were used for further analysis. Alignments were extended in silico at their 3'ends to a length of 200 bp and assigned to 32-nt bins along the genome. The resulting histograms (genomic "signal maps") were stored in the bigWig files. Peaks were identified using the MACS 2.1.0 algorithm at a cutoff of *P*-value 1.0 $\times 10^{-7}$, without the control file, and with the –nomodel option. Peaks on the ENCODE blacklist of known false ChIP-Seq peaks were excluded. Signal maps and peak locations were used as input data for Active Motif's proprietary analysis program, which creates Excel tables containing detailed information on sample comparisons, peak metrics, peak locations, and gene annotations. For differential analysis, reads were counted in all merged peak regions (using Subread) and the replicates for each condition were compared using DESeq2. IGV was used to visualize the raw intensities[112]. Statistical analyses were performed using an in-house R script, unless otherwise specified.

Immunohistochemistry

Immunostaining of brain sample with PFA fixation

812 The mice were deeply anesthetized with isoflurane and transcardially perfused with PBS,
813 followed by 4% PFA in PBS. Brains were dissected, immersed overnight in 4% PFA in PBS,
814 and cryoprotected by incubation in 20% sucrose in PBS for three days at 4℃. After
815 cryoprotection, the brains were mounted in Tissue-Tek optimal cutting temperature compound
816 (Miles, Elkhart, IN) and frozen in liquid nitrogen. Brain samples were cut into 10-μm-thick
817 coronal sections using a microtome (CM1850; Leica Microsystems, Wetzlar, Germany). The
818 sections were stained with the following antibodies: Calbindin (1:1000, rabbit, polyclonal,
819 Synaptic Systems Cat# 214 002, RRID:AB_2068199), Cyclin B (1:500, mouse, monoclonal,
820 Thermo Fisher Scientific Cat# MA1-155, RRID:AB_2536863), phospho-Histone H3 (1:500,
821 rabbit, polyclonal, Millipore Cat# 06-570, RRID:AB_310177), HA-tag (1:500, rabbit,
822 polyclonal, Cell Signaling Technology Cat# 3724, RRID:AB_1549585), ΔFosB (1:1000, rabbit,
823 monoclonal, Cell Signaling Technology Cat# 14695, RRID:AB_2798577), Calbindin (1:1000,
824 rabbit, polyclonal, Synaptic Systems Cat# 214002, RRID:AB_2068199), NeuN (1:500, mouse,
825 monoclonal, Millipore, Cat# MAB377X, RRID:AB_2149209), GFAP (1:500, rabbit,
826 polyclonal, Sigma-Aldrich, Cat# G9269, RRID:AB_477035), Iba1 (1:500, rabbit, polyclonal,
827 FUJIFILM, Cat# 019-19741, RRID:AB_839504), JunD (1:500, rabbit, polyclonal, Abcam,
828 Cat# ab28837, RRID:AB_2130167), and tri-methyl-Histone H3 (Lys9me3) (1:500, mouse,
829 monoclonal, FUJIFILM Cat# MABI0308). Before the first antibody reaction, antigen retrieval
830 was performed in 120℃ autoclave for 5 minutes in 0.01 M sodium citrate buffer (S1699,
831 Target Retrieval Solution, Dako). Autoclave at 120℃ is essential, especially for detecting
832 weak signals of nuclear antigens (e.g., pH3 and Cyclin B). This procedure also eliminates
833 EYFP/mCherry fluorescence, thus preventing overlap with secondary antibody staining with
834 Alexa 488/594. After antigen retrieval, sections were cooled at room temperature for 2 hours.
835 Sections were pre-incubated for 1 hour at room temperature in 5% skim milk in PBST for
836 blocking, and then incubated overnight at 4℃ in PBS containing the primary antibodies. The
837 next day, secondary antibody reactions were performed for 1 hour at room temperature using
838 Alexa Fluor 488-, Alexa Fluor 594-, and Alexa Fluor 647-conjugated secondary antibodies
839 (Invitrogen). Nuclear staining was performed using Hoechst 33258 (Polysciences, Warrington,
840 PA).
841
842 *Immunostaining of brain sample with acetone fixation*
843 For Lamin B1 staining (1:200, mouse, monoclonal, Thermo Fisher Scientific Cat# MA1-06103,
844 RRID:AB_2281281), a method omitting PFA perfusion was employed[113,114]. In this protocol,
845 brains were perfused with PBS alone, without PFA. Immediately after PBS perfusion, the
846 dissected brains were mounted in Tissue-Tek compound and frozen in liquid nitrogen. Brain

847 samples were cut into 10-μm-thick coronal sections using a microtome. Before the first
848 antibody staining, the brain sections were fixed with ice-cold acetone. Antigen retrieval before
849 the blocking step was omitted and subsequent procedures were performed in the same manner
850 as for immunostaining of the fixed brain samples.
851
852 *TUNEL staining*
853 In Situ Cell Death Detection Kit TMR red (Roche, 12156792910) was used for the detection
854 of apoptotic cells. Brain sections were rinsed in PBS, permeabilized with 0.1 % Tween for 30
855 min, and incubated with TUNEL reaction reagent (TdT Enzyme and Labeling Safe Buffer) and
856 Hoechst for 60 min at room temperature. Embryo brain tissue was used as the positive control.
857 The localization of TUNEL to the nucleus allows for accurate counting of dead or dying cells.
858
859 *Image acquisition and analysis*
860 Confocal microscopy (LSM 700; Zeiss) was used to obtain images of stained sections. For
861 image analysis, the regions of interest (ROIs) were manually delineated using ZEN (Zeiss) and
862 ImageJ software.
863
864
865
866 ***Behavioral tests***
867
868 *Open field test*
869 The open field test was performed in an open field apparatus (40 cm × 40 cm × 30 cm; width,
870 depth, and height, respectively; O'Hara, Japan) made of opaque white plastic, with the center
871 area illuminated to 100 lux by an LED light attached above the ceiling. Before each behavioral
872 experiment, the open field apparatus was cleaned with weakly acidified hypochlorous water
873 (super-hypochlorous water; Shimizu Laboratory Supplies, Kyoto, Japan) to prevent bias due to
874 olfactory cues. All behavioral experiments were conducted in a soundproof room. During each
875 recording session, mouse movements were captured using a CCD camera above the open field
876 arena. Mouse behavior was monitored using a computer screen located outside the room to
877 minimize artifacts caused by the experimenter's presence. Mouse behavior was recorded at a
878 sampling rate of 10 Hz. Mouse images were automatically processed using the ImageJ plugin
879 (Image OF, freely available on the Mouse Phenotype Database website: http://www.mouse-
880 phenotype.org/software.html) to obtain the location-time sequence for each mouse. From the
881 traces of mouse movements, we calculated the total distance traveled by the mice during the

882 session[115].
883
884 *Locomotor activity monitoring in home cage*
885 Locomotor activity monitoring was performed on mice that had been operated at least one
886 month before. The system automatically analysed the locomotor activity of the mice in their
887 home cage[116]. The system contains a home cage (29 × 18 × 12 cm) and a filtered cage top,
888 separated by a 13-cm-high metal stand containing an infrared video camera, which is attached
889 to the top of the stand. Each mouse was individually housed in each home cage, and their
890 locomotor activity was monitored 24 hours a day. Outputs from the video cameras were fed
891 into a computer and images from each cage were captured at a rate of one frame per second.
892 The distance traveled was calculated automatically using the ImageJ plugin[115].
893
894 *Tail suspension test*
895 The tail suspension test was performed to assess depression-related behavior in mice. Each
896 mouse was suspended 30 cm above the floor by the tail in a white plastic chamber (44 cm
897 height × 49 cm length × 32 cm width; O'Hara, Japan) with a video camera mounted on the wall
898 (O'Hara, Japan). The behavior was recorded for 10 minutes. Images were captured at two
899 frames per second using a video camera and transferred to a computer. The area (pixels) within
900 which the mouse moved was measured for each pair of successive frames. When the area was
901 below a certain threshold, the mouse behavior was judged as "immobile." When the area
902 equaled or exceeded the threshold, the mouse was considered "moving." The optimal threshold
903 for this judgment was determined by adjusting it to the amount of immobility measured by a
904 trained human observer. Immobility lasting for < 2 seconds was not included in the analysis.
905 Data acquisition and analysis were performed automatically using the ImageJ plugin
906 software[115].
907
908 *Porsolt forced swim test*
909 The Porsolt forced swim test was performed to assess depression-related behavior. A Plexiglas
910 cylinder (20 cm height × 10 cm diameter) was placed in a test chamber (49 cm height × 44 cm
911 length × 32 cm width; O'Hara, Japan). A video camera was mounted on the ceiling of the test
912 chamber and positioned directly above the cylinder. The mice were placed into a cylinder,
913 which was filled with water (approximately 23°C) to a height of 7.5 cm.
914 The immobility time was recorded for 10 minutes. Images were captured at two frames per
915 second through the video camera. The immobility status of each mouse was determined in the
916 same manner as for the tail suspension test. Data acquisition and analysis were performed using

917 the ImageJ plugin[115].
918
919 *Contextual and cued fear-conditioning tests*
920 Fear conditioning tests were conducted to assess contextual memory (Extended Data Fig. 3a).
921 In the conditioning session, each mouse was placed in an acrylic chamber consisting of white
922 (side) and transparent (front, rear, and top) walls (33 × 25 × 28 cm) with a stainless-steel grid
923 floor (0.2 cm diameter, spaced 0.5 cm apart; O'Hara, Japan). The mice were allowed to explore
924 the chamber freely for 120 seconds, and 55 dB white noise then served as the conditioned
925 stimulus (CS) for 30 seconds. During the last 2 seconds of CS presentation, a mild foot shock
926 (0.3 mA, 2 seconds) was delivered as the unconditioned stimulus (US). The mice were
927 subjected to two more CS-US pairings with a 2-minutes interstimulus interval. Approximately
928 24 hours or one month after conditioning, a context test was conducted for 300 seconds. In the
929 context test, mice were placed in the same chamber in which they had been conditioned. After
930 the context test, a cued test with an altered context was performed for 360 seconds. In the cued
931 test, the mice were placed in a triangular chamber (33 × 29 × 32 cm) made of white plastic
932 walls and floor, which was located in a different sound-attenuating room and allowed to explore
933 the triangular chamber for 180 seconds. Then, the CS was presented during the last 180 seconds
934 of the cued test. In each session, the percentage of freezing and distance traveled was calculated
935 automatically using the ImageJ plugin[115].
936
937 *Three chamber social interaction test*
938 The testing apparatus consisted of a rectangular three-chambered box and lid with a video
939 camera (O'Hara, Japan; Extended Data Fig. 3b). The dividing walls of the chamber were made
940 of transparent plastic, with small square openings (5 × 3 cm) allowing access to each chamber
941 (20 × 40 × 47 cm). A small round wire cage (9 cm in diameter, 11 cm in height, with vertical
942 bars 0.5 cm apart) was located in the corner of chambers. The test mice were first placed in the
943 middle chamber and allowed to explore the entire test chamber for 10 minutes. Immediately
944 after the 10-minute period, the test mice were placed in a clean holding cage, and a male
945 C57BL/6J mouse (stranger mouse) with no prior contact with the test mice was enclosed in
946 one of the wire cages. The test mice were returned to the middle chamber and allowed to
947 explore for 10 minutes. The time spent in each chamber and the time spent around each cage
948 was automatically measured using ImageCSI software[115].
949
950
951

952 ***in vivo Ca^{2+} imaging with optogenetic stimulation***

953

954 *Viral constructs*

955 Purified and concentrated adeno-associated virus serotype 5 coding GCaMP6f under the
956 synapsin promoter (AAV5-syn-GCaMP6f; #100837-AAV5) and adeno-associated virus
957 serotype 5 coding for ChrimsonR-tdTomato under the synapsin promoter (AAV5-syn-
958 ChrimsonR-tdT) were obtained from Addgene and UNC Vector Core Facility.

959

960 *Viral delivery of Ca^{2+} sensor and opsin*

961 For delivery of a fluorescent Ca^{2+} sensor and red-shifted opsin into dDG neurons, AAV5-syn-
962 GCaMP6f and AAV5-syn-ChrimsonR-tdT were injected into the dorsal DG in adult mice (left
963 hemisphere; 2.0 mm posterior to bregma [AP], 1.0–1.45 mm lateral to midline [ML], and 2.0
964 mm ventral to bregma [DV]). Briefly, adult mice (> 8 weeks old) were anesthetized with 1.5
965 to 3% isoflurane at an oxygen flow rate of 1 L/min. The head fur was shaved and the incision
966 site was sterilized with 70% ethanol prior to the surgical procedure. Mice were mounted on a
967 stereotaxic device (catalog no. 51730D, Stoelting), and heat pad (catalog no. BWT-100A,
968 BRC) was placed underneath each mouse to maintain body temperature at 37 °C. After the
969 scalp was incised and pulled aside, a 2-mm-diameter craniotomy was created with a surgical
970 drill on the skull above the injection site. Through a glass-capillary injection pipette (25-µm
971 inner-diameter tip), a mixture of 300nl of AAV5-Syn-GCaMP6f-WPRE-SV40 (titer 4.3×10^{12}
972 GC/mL) and AAV5-syn-ChrimsonR-tdT (titer 1.53×10^{12} GC/mL) was injected using a
973 microinjection pump (Nanoliter 2010, WPI). After the injection, the scalp was sutured and
974 treated with povidone–iodine. The expression of GCaMP6f is driven by the Syn promoter and
975 is expected to be induced not only in GCs but also in other cell types. We previously reported
976 that the majority (approximately 90%) of neurons expressing GCaMP in the DG are GCs[16].

977

978 *GRIN lens implantation*

979 At least two weeks after viral injection, a gradient refractive index (GRIN) lens (Inscopix
980 catalog no.1050-004623, 1 mm diameter) was implanted at the same position where the virus
981 was injected. The mouse was mounted on a stereotaxic device and the scalp was removed.
982 After exposing the skull and removing the overlying connective tissue, we made a cranial hole
983 slightly larger than the diameter of the GRIN lens. To secure for an entry path for the GRIN
984 lens, the cortex and white matter were aspirated using a 26-gauge blunt needle attached to a
985 vacuum pump; to prevent aspiration of the GCs, the depth of needle tip depth was set at 1.6
986 mm from the bregma and the tissue below was carefully aspirated. Saline was continuously

applied during aspiration to prevent the tissue from drying. During implantation, the lenses were held in place and slowly lowered using a ProView Implant kit (nVoke, Inscopix, Palo Alto, California, USA) attached to the stereotaxic arm. The GRIN lens connected to the manual stereotaxic arm was slowly lowered (5–10 μm/sec) until the field of view was in focus, referring to the fluorescence intensity of the GCaMP. After temporarily immobilizing the lens with ultraviolet-curable resin (Primefil, Tokuyama Dental), it was fixed to the exposed skull using dental cement（Super-Bond C&B, Sun Medical）. The exposed tip of the GRIN lens was covered with dental silicone (Dent Silicone-V, Shofu). After lens implantation, analgesic and anti-inflammatory agents (Flunixin, 2 mg/kg; Fujita) and antibiotics (Tribrissen, 0.12 mL/kg; Kyoritsu Seiyaku) were injected intraperitoneally.

Baseplate attachment

At least two weeks after GRIN lens implantation, the baseplate of a miniature microendoscope (nVoke, Inscopix) was attached to the GRIN lens using a previously described method[16]. Briefly, the mice were anesthetized and mounted onto a stereotaxic device, and a baseplate attached to the miniature microscope was placed on the GRIN lens using a gripper (nVoke accessory, Inscopix). The optimal location was determined by monitoring the fluorescent images of GCaMP-expressing neurons (where the largest number of neurons was in focus), and the baseplate was fixed with ultraviolet-curable resin and dental cement at this position. In cases where we failed to identify neurons at this stage (usually due to the failure of GRIN-lens implantation), the baseplate was not attached, and such mice were excluded from the experiment. After the baseplate attachment, a baseplate cover was placed on the baseplate until Ca^{2+} imaging was performed.

Ca^{2+} imaging and optogenetic stimulation in freely moving mice

Ca^{2+} imaging of the DG neurons was performed while the mice traveled freely in the OF. Prior to Ca^{2+} imaging, the mice were lightly anesthetized and a miniature microscope (nVoke, Inscopix) was mounted onto the baseplate of the mice. The mice were then placed back in their home cages and transferred to a sound-proof behavioral experiment room. At least 30 min after recovery from anesthesia, the mice were subjected to OF. The Ca^{2+} signals of their DG neurons were obtained at a 10-Hz sampling rate with a 1,440×l,080-pixel resolution. Recordings per day totaled 50 min, consisting of before (0–30 min), during (30–35 min), and after (35–50 min) optogenetic stimulation; no stimulation was introduced in the control group. These 50-min recordings were performed daily throughout the experimental period, and the first 30 min recordings were used for data analysis. The experimental period consisted of before stimulation

1022 (Day 1), during stimulation (Day 2-11), and two weeks after stimulation (Day 24-26). We
1023 applied EX-LED (filtered with a 435–460 nm excitation filter) for the excitation of GCaMP6f
1024 fluorescence (0.4 mW/mm^2 at the bottom of the GRIN lens) and OG-LED (filtered with a 590–
1025 650 nm excitation filter) for the excitation of ChrimsonR (10 mW/mm^2 at the bottom of the
1026 GRIN lens). A previous study reported that EX-LED at 2.0 mW/mm^2 resulted in small current
1027 changes of approximately 10 pA via activation of ChrimsonR under slice preparation
1028 (approximately 130 pA by OG-LED irradiation)[117]. Given that EX-LED used in this study are
1029 much lower than these conditions (–0.4 mW/mm^2) and that under *in vivo* imaging conditions
1030 the EX-LED are scattered in the brain tissue and the current changes are much smaller than in
1031 slice preparation[117], unintended activation of ChrimsonR by EX-LED would be negligible.
1032
1033 *Detection of Ca^{2+} transients*
1034 To extract the activity patterns of individual DG neurons from the obtained fluorescent images,
1035 we used Inscopix Data Processing Software (IDPS 1.8.0). Briefly, the data files of the raw
1036 sequential fluorescent images obtained by nVoke (Inscopix) were imported to the IDPS, and
1037 movie trimming, data preprocessing, spatial filtering, and motion correction were applied. The
1038 instantaneous fluorescence of the motion-corrected images was then normalized by its average
1039 fluorescence over the entire recording period, producing fluorescence-change ratio ($\Delta F/F$)
1040 images. Individual DG neurons were identified using the automated principal component
1041 analysis (PCA) and independent component analysis (ICA) segmentation of activity traces. For
1042 PCA/ICA segmentation, default parameters, whose values were confirmed to work well across
1043 most of the neuronal activity patterns in the cortex and CA1 of the hippocampus, were used
1044 (number of independent components, 120; number of principal components, 150; ICA max
1045 iterations, 100; ICA random seed, 0; ICA convergence threshold, 0.00001; block size, 1,000;
1046 ICA unmixing dimension, spatial; ICA temporal weights, 0.00; and arbitrary units within the
1047 IDPS). Finally, the temporal pattern of each timing of DG neuron activity was identified by an
1048 event-detection algorithm available in IDPS (event threshold factor, four median absolute
1049 deviations; event shortest decay time, 0.2 s), and the temporal pattern of activity was expressed
1050 as a time series of binarized signals for further analysis.
1051
1052
1053
1054 ***Information coding in individual neurons***
1055
1056 *Definitions of the position and speed of mice*

(i) Position: The OF arena (which had an area of 40 cm × 40 cm) was represented as 200 × 200-pixel grid. The position of the mouse was determined from the centroid of its shadow on the CCD camera, above the OF. We then assigned a label corresponding to the discrete location of the mouse (e.g., [10, 100]) to each time bin (=1/10sec).

(ii) Speed: From the distance traveled between 1 s before and after a given time point, we calculated the speed of the mouse at that moment and assigned this speed (cm/s) to each time bin.

Statistical analysis of spatial and speed information

To quantify the tuning specificities of neurons with respect to the position and speed of the mouse, we measured their specificity in terms of the information rate of cell activity, and defined them as (i) spatial and (ii) speed information[16,118]. The Ca^{2+} event rate in Ca^{2+} imaging was considerably lower than that in electrophysiological recordings (average, approximately 0.05 Hz). If the discretization of position and speed is too fine for the number of events in the recorded cells, a proper null distribution cannot be obtained when creating shuffled data for that cell. Therefore, we set the resolution of the discretization of the position and speed to be lower than those that are commonly used.

(i) We used a 2×2 square grid to measure spatial information and computed the amount of Shannon information conveyed by a single Ca^{2+} transient about the animal's position. The spatial information I (bits per Ca^{2+} transient) of a cell was calculated as the mutual information score between the occurrence of a single Ca^{2+} transient in the cell and the animal's behavioral state of position using the following formula:

$$I_{(\mathrm{bits/Ca^{2+}\ transient})} = \sum_{i=1}^{N} p_i \frac{r_i}{r} \log_2 \frac{r_i}{r}$$

where i is the bin number corresponding to the physical parameter (in this case, spatial position in the OF; i = 1–4 from the 2×2 square grid), N is the total number of bins, p is the probability that the mouse occupied bin i, r_i is the mean transient rate at bin i, and r is the overall mean transient rate.

(ii) To measure speed information, we applied the same formula to the speed after discretizing it to a binary state: Run (speed > 1 cm/sec) and Stop (speed < 1 cm/sec).

Definitions of place cells and speed cells

To evaluate the statistical significance of the information encoded in individual neurons, we employed the random permutation method as previously outlined[16]. The calcium event data

1090 were divided into 1000 segments along the time axis and randomly shuffled to generate
1091 permuted calcium event data. This method disrupts the temporal structures of neural activity
1092 and the temporal correlations between neural activity and behavioral variables. Using this
1093 randomly permuted data, we derived a null distribution for the position and speed information
1094 of neurons. Neurons with original information content exceeding the top 95% and 99% of these
1095 null distributions were classified as place or speed cells, respectively, indicating cells with
1096 significant spatial or speed information[119,120].
1097
1098
1099
1100 ***Decoding position and speed in the open field***
1101 To determine how OF behavioral parameters are encoded in the population activities of DG
1102 neurons, we trained decoders using machine learning methods to predict the position and speed
1103 of mice from the population Ca^{2+} activity. We assigned labels to the discretized behavioral
1104 parameters of the mouse (position (cm) and speed (cm/s)) and the binary values of the Ca^{2+}
1105 signal (0 or 1) of all neurons in each time bin. We then divided the Ca^{2+} imaging data and
1106 behavioral data of the first 30 min (before 5-min of optogenetic stimulation each day) into the
1107 first 15 min and last 15 min halves, which were designated as training and test data, respectively.
1108 For each pair of behavioral parameters (position and speed) and the value of the Ca^{2+} signal in
1109 the training data, we trained the decoders using a machine learning method (the code was
1110 obtained and modified from Glaser *et al*., eNeuro, 2020[121]). The decoding accuracy of the
1111 position was reported as the mean absolute error of the distance between the predicted and
1112 actual positions. In the case of speed, decoding accuracy was reported as the correlation
1113 between the predicted and actual instantaneous speeds. This is because speed, unlike position,
1114 is not limited to a certain range and the mean absolute error of speed depends on the average
1115 locomotion speed of each mouse, which is inappropriate for the evaluation of the decoding
1116 error. If the number of neurons recorded in each session was less than 10, the session was
1117 excluded from the decoding analysis.
1118
1119
1120
1121 ***DNA Constructs and AAV Vectors for in vivo genome editing***
1122 For SpCas9 target selection and single-guide RNA (sgRNA) generation, 20-nt target sequences
1123 were selected to precede a 5'-NGG protospacer-adjacent motif (PAM) sequence. To minimize
1124 off-target effects, CRISPR design tool was used (https://crispr.dbcls.jp/). The backbone

1125 plasmid for sgRNA (PX552; pAAV-U6sgRNA(SapI)_hSyn-GFP-KASH-bGH) was obtained
1126 from Addgene. *Ccnb*-sgRNA (*Ccnb1* and *Ccnb2* were tandemly connected; Fig. 5b) and
1127 *Scramble*-sgRNA nucleotides were synthesized and cloned into AAV backbone plasmids
1128 (Vigene Biosciences, Inc, USA). To avoid fluorescence overlap with ChR2-EYFP, the GFP
1129 cassette was replaced with mCherry (Fig. 5b). The plasmid for SpCas9 was obtained from
1130 Addgene (PX551; pAAV-pMecp2-SpCas9-spA). Concentrated AAV vectors were produced
1131 from plasmids for *Ccnb*-sgRNA, *Scramble*-gRNA, and SpCas9, with support from the Gunma
1132 University Initiative for Advanced Research Viral Vector Core.
1133
1134
1135
1136 ***Stimulated Emission Depletion Microscopy (STED) observation***
1137 Brain slices were double-immunostained with anti-tri-methyl-Histone H3 (Lys9me3) antibody
1138 (1:500, mouse, monoclonal, MAI0308, FUJIFILM) and anti-phospho-Histone H3 antibody
1139 (1:500, rabbit, polyclonal #06-570, Cell Signaling) as the primary antibodies, followed by
1140 Alexa Fluor 488- and Alexa Fluor 555- conjugated antibodies (Molecular Probes) as the
1141 secondary antibodies. STED images were acquired using a TCS SP8 STED 3X system (Leica
1142 Microsystems, Wetzlar, Germany) with 2ch HyDSMD detectors[122]. A white laser (for
1143 excitation) and a 660 nm laser with a donut beam (for stimulated emission depletion) were used
1144 for STED imaging. For the detection of signals of tri-methyl-Histone H3 (Lys9me3) and
1145 phospho-Histone H3, we used excitation wavelengths of 488 and 561 nm, respectively. Raw
1146 STED images (pixel size:20 nm) were recorded with a 93 × glycerol immersion objective
1147 (Leica HC PL APO 93 × /1.30 GLYC motC STED W) and deconvoluted using the Huygens
1148 software (SVI, Hilversum, Netherlands). Image analysis was performed with a custom-
1149 developed code using the image processing toolbox in MATLAB (MathWorks, R2022a).
1150
1151
1152
1153 ***Data Collection, Pre-processing, and Meta-analysis***
1154 All microarray and RNA-seq data used for meta-analysis in this study were obtained from the
1155 BaseSpace Correlation Engine (https://japan.ussc.informatics.illumina.com/c/nextbio.nb;
1156 Illumina, Cupertino, CA), a publicly available database containing over 100,000 microarray
1157 and RNA-seq datasets. The details of all datasets are described in Supplementary Table1. The
1158 datasets registered in BaseSpace underwent several preprocessing, quality control, and
1159 organization stages. Quality control ensures the integrity of samples and datasets. Genes with

a P value < 0.05 (without correction for multiple testing) were included in the differentially expressed gene datasets. This sensitivity threshold is typically the lowest used with commercial microarray platforms and the default criterion in BaseSpace analyses[44]. Correction for multiple testing was omitted to minimize false negatives at this stage. Expression values were used to calculate fold changes and P values between the two conditions (infants–adults and treated–untreated). To determine fold changes, we divided the expression values of the probes/genes in the test datasets by those in the control datasets. If the fold change was < 1.0, these values were converted to a negative reciprocal or −1/(fold change). Genes with a t-test P value < 0.05 were imported into the BaseSpace Correlation Engine according to the instructions provided by the manufacturer. The rank order of these genes was determined based on their absolute fold-changes. All meta-statistical analyses comparing two datasets were performed in BaseSpace, and the similarities between any two datasets were evaluated as overlap P values using the Running Fisher algorithm[44].

Statistical Analyses

Mice of the same age and sex were raised under identical conditions and were randomly allocated to different experimental groups. Blinding was not applied in this study because the animals needed to be controlled by the stimulation conditions. The sample sizes were determined based on those reported in similar publications[30,31]. Welch's t-test was used to compare the averages. An ANOVA was performed when more than two groups were compared, followed by the Bonferroni post-hoc method. For correlation analysis, we used Pearson correlation analysis for normally distributed data. When pooling the data of neurons from multiple mice per group, a Linear Mixed-Effects Regression model was applied to account for individual differences per mouse. All results of the statistical analyses are summarized in Supplementary Table 2.

Code and Data Availability

RNA-seq and ATAC-seq data used in this study were deposited in the GEO database with accession codes GSE227200 (RNAseq) and GSE227201 (ATAC-seq), respectively. The RNA-seq data for the post-mortem DG of human patient was obtained from SRP241159. The personal information regarding ECT history was provided by Astellas Pharma Inc. The raw

imaging data were uploaded to the Systems Science Biological Dynamics repository (https://ssbd.riken.jp/repository/335). The confocal images used in the analysis were uploaded to a figshare with DOI (https://doi.org/10.6084/m9.figshare.28853303). The codes and processed data supporting the findings of this study are available at https://github.com/tmurano. Additional information is available from the corresponding authors upon request.

1201 1. Choi, D. W. Excitotoxic cell death. *Journal of Neurobiology* **23**, 1261–
1202 1276 (1992).
1203 2. Dong, X., Wang, Y. & Qin, Z. Molecular mechanisms of excitotoxicity
1204 and their relevance to pathogenesis of neurodegenerative diseases. *Acta Pharmacol Sin* **30**,
1205 379–387 (2009).
1206 3. Singh, S. P., He, X., McNamara, J. O. & Danzer, S. C. Morphological
1207 changes among hippocampal dentate granule cells exposed to early kindling-epileptogenesis.
1208 *Hippocampus* **23**, 1309–1320 (2013).
1209 4. Lepeta, K. *et al.* Synaptopathies: synaptic dysfunction in neurological
1210 disorders – A review from students to students. *Journal of Neurochemistry* **138**, 785–805
1211 (2016).
1212 5. Holmes, G. L. & Ben-Ari, Y. The Neurobiology and Consequences of
1213 Epilepsy in the Developing Brain. *Pediatr Res* **49**, 320–325 (2001).
1214 6. Pan, G. *et al.* Compensatory Mechanisms Modulate the Neuronal
1215 Excitability in a Kainic Acid-Induced Epilepsy Mouse Model. *Frontiers in Neural Circuits* **12**,
1216 (2018).
1217 7. Hagihara, H., Takao, K., Walton, N. M., Matsumoto, M. & Miyakawa, T.
1218 Immature dentate gyrus: an endophenotype of neuropsychiatric disorders. *Neural Plasticity*
1219 **2013**, e318596 (2013).
1220 8. Shin, R. *et al.* The immature dentate gyrus represents a shared phenotype
1221 of mouse models of epilepsy and psychiatric disease. *Bipolar Disorders* **15**, 405–421 (2013).
1222 9. Imoto, Y., Segi-Nishida, E., Suzuki, H. & Kobayashi, K. Rapid and stable
1223 changes in maturation-related phenotypes of the adult hippocampal neurons by
1224 electroconvulsive treatment. *Mol Brain* **10**, 8 (2017).
1225 10. Ueno, M. *et al.* The effect of electroconvulsive seizure on survival,
1226 neuronal differentiation, and expression of the maturation marker in the adult mouse
1227 hippocampus. *J. Neurochem.* (2019) doi:10.1111/jnc.14691.
1228 11. Murano, T., Hagihara, H., Tajinda, K., Matsumoto, M. & Miyakawa, T.
1229 Transcriptomic immaturity inducible by neural hyperexcitation is shared by multiple
1230 neuropsychiatric disorders. *Commun Biol* **2**, 1–11 (2019).
1231 12. Yamasaki, N. *et al.* Alpha-CaMKII deficiency causes immature dentate
1232 gyrus, a novel candidate endophenotype of psychiatric disorders. *Molecular Brain* **1**, 6 (2008).
1233 13. Takao, K. *et al.* Deficiency of Schnurri-2, an MHC Enhancer Binding
1234 Protein, Induces Mild Chronic Inflammation in the Brain and Confers Molecular, Neuronal,
1235 and Behavioral Phenotypes Related to Schizophrenia. *Neuropsychopharmacology* **38**, 1409–

1425 (2013).

14. Umemori, J., Winkel, F., Didio, G., Pou, M. L. & Castrén, E. iPlasticity: Induced juvenile-like plasticity in the adult brain as a mechanism of antidepressants. *Psychiatry Clin Neurosci* **72**, 633–653 (2018).

15. Hagihara, H. *et al.* Forebrain-specific conditional calcineurin deficiency induces dentate gyrus immaturity and hyper-dopaminergic signaling in mice. *Molecular Brain* **15**, 94 (2022).

16. Murano, T. *et al.* Multiple types of navigational information are independently encoded in the population activities of the dentate gyrus neurons. *Proceedings of the National Academy of Sciences* **119**, e2106830119 (2022).

17. Hagihara, H. *et al.* Large-scale animal model study uncovers altered brain pH and lactate levels as a transdiagnostic endophenotype of neuropsychiatric disorders involving cognitive impairment. *eLife* **12**, RP89376 (2024).

18. Li, B. *et al.* Failure of Neuronal Maturation in Alzheimer Disease Dentate Gyrus. *J Neuropathol Exp Neurol* **67**, 78–84 (2008).

19. Walton, N. M. *et al.* Detection of an immature dentate gyrus feature in human schizophrenia/bipolar patients. *Transl Psychiatry* **2**, e135 (2012).

20. Hagihara, H., Ohira, K., Takao, K. & Miyakawa, T. Transcriptomic evidence for immaturity of the prefrontal cortex in patients with schizophrenia. *Molecular Brain* **7**, 41 (2014).

21. You, J. C. *et al.* Epigenetic suppression of hippocampal calbindin-D28k by ΔFosB drives seizure-related cognitive deficits. *Nature Medicine* **23**, 1377 (2017).

22. Murano, T., Koshimizu, H., Hagihara, H. & Miyakawa, T. Transcriptomic immaturity of the hippocampus and prefrontal cortex in patients with alcoholism. *Sci Rep* **7**, 44531 (2017).

23. Tavitian, A., Song, W. & Schipper, H. M. Dentate Gyrus Immaturity in Schizophrenia. *Neuroscientist* 1073858418824072 (2019) doi:10.1177/1073858418824072.

24. May, A. Experience-dependent structural plasticity in the adult human brain. *Trends in Cognitive Sciences* **15**, 475–482 (2011).

25. Ganguly, K. & Poo, M. Activity-Dependent Neural Plasticity from Bench to Bedside. *Neuron* **80**, 729–741 (2013).

26. Malenka, R. C. & Bear, M. F. LTP and LTD: An Embarrassment of Riches. *Neuron* **44**, 5–21 (2004).

27. Citri, A. & Malenka, R. C. Synaptic Plasticity: Multiple Forms, Functions, and Mechanisms. *Neuropsychopharmacol* **33**, 18–41 (2008).

28. Zhang, W. & Linden, D. J. The other side of the engram: experience-driven changes in neuronal intrinsic excitability. *Nat Rev Neurosci* **4**, 885–900 (2003).

29. Titley, H. K., Brunel, N. & Hansel, C. Toward a Neurocentric View of Learning. *Neuron* **95**, 19–32 (2017).

30. Su, Y. *et al.* Neuronal activity modifies the chromatin accessibility landscape in the adult brain. *Nat Neurosci* **20**, 476–483 (2017).

31. Fernandez-Albert, J. *et al.* Immediate and deferred epigenomic signatures of in vivo neuronal activation in mouse hippocampus. *Nature Neuroscience* **22**, 1718–1730 (2019).

32. Espinoza, R. T. & Kellner, C. H. Electroconvulsive Therapy. *New England Journal of Medicine* **386**, 667–672 (2022).

33. Salik, I. & Marwaha, R. Electroconvulsive Therapy. in *StatPearls* (StatPearls Publishing, Treasure Island (FL), 2024).

34. Oltedal, L. *et al.* Volume of the Human Hippocampus and Clinical Response Following Electroconvulsive Therapy. *Biological Psychiatry* **84**, 574–581 (2018).

35. Nuninga, J. O. *et al.* Volume increase in the dentate gyrus after electroconvulsive therapy in depressed patients as measured with 7T. *Molecular Psychiatry* **25**, 1559–1568 (2020).

36. Loef, D. *et al.* Electroconvulsive therapy is associated with increased immunoreactivity of neuroplasticity markers in the hippocampus of depressed patients. *Transl Psychiatry* **13**, 1–11 (2023).

37. Zhao, C., Warner-Schmidt, J., S. Duman, R. & Gage, F. H. Electroconvulsive seizure promotes spine maturation in newborn dentate granule cells in adult rat. *Devel Neurobio* **72**, 937–942 (2012).

38. Kobayashi, K. *et al.* Rapid and lasting enhancement of dopaminergic modulation at the hippocampal mossy fiber synapse by electroconvulsive treatment. *Journal of Neurophysiology* **117**, 284–289 (2017).

39. Kobayashi, K. *et al.* Reversal of hippocampal neuronal maturation by serotonergic antidepressants. *Proc. Natl. Acad. Sci. U.S.A.* **107**, 8434–8439 (2010).

40. Ohira, K., Hagihara, H., Miwa, M., Nakamura, K. & Miyakawa, T. Fluoxetine-induced dematuration of hippocampal neurons and adult cortical neurogenesis in the common marmoset. *Mol Brain* **12**, 69 (2019).

41. Nguyen, P. T. *et al.* Antidepressants reactivate developmental plasticity through remodeling of extracellular matrix. 2025.01.03.631260 Preprint at https://doi.org/10.1101/2025.01.03.631260 (2025).

1306 42. Lefaucheur, J.-P. *et al.* Evidence-based guidelines on the therapeutic use
1307 of repetitive transcranial magnetic stimulation (rTMS): An update (2014–2018). *Clinical*
1308 *Neurophysiology* **131**, 474–528 (2020).
1309 43. Shiozawa, P. *et al.* Transcranial direct current stimulation for major
1310 depression: an updated systematic review and meta-analysis. *International Journal of*
1311 *Neuropsychopharmacology* **17**, 1443–1452 (2014).
1312 44. Kupershmidt, I. *et al.* Ontology-Based Meta-Analysis of Global
1313 Collections of High-Throughput Public Data. *PLoS ONE* **5**, e13066 (2010).
1314 45. Jaffe, A. E. *et al.* Profiling gene expression in the human dentate gyrus
1315 granule cell layer reveals insights into schizophrenia and its genetic risk. *Nat Neurosci* 1–10
1316 (2020) doi:10.1038/s41593-020-0604-z.
1317 46. Kang, H. J. *et al.* Spatio-temporal transcriptome of the human brain.
1318 *Nature* **478**, 483–489 (2011).
1319 47. Klemm, S. L., Shipony, Z. & Greenleaf, W. J. Chromatin accessibility and
1320 the regulatory epigenome. *Nat Rev Genet* **20**, 207–220 (2019).
1321 48. Kheirbek, M. A. *et al.* Differential Control of Learning and Anxiety along
1322 the Dorsoventral Axis of the Dentate Gyrus. *Neuron* **77**, 955–968 (2013).
1323 49. Stefanini, F. *et al.* A Distributed Neural Code in the Dentate Gyrus and in
1324 CA1. *Neuron* (2020) doi:10.1016/j.neuron.2020.05.022.
1325 50. Whitfield, M. L. *et al.* Identification of Genes Periodically Expressed in
1326 the Human Cell Cycle and Their Expression in Tumors. *MBoC* **13**, 1977–2000 (2002).
1327 51. Dechat, T. *et al.* Nuclear lamins: major factors in the structural
1328 organization and function of the nucleus and chromatin. *Genes Dev.* **22**, 832–853 (2008).
1329 52. Gruenbaum, Y. & Foisner, R. Lamins: nuclear intermediate filament
1330 proteins with fundamental functions in nuclear mechanics and genome regulation. *Annu Rev*
1331 *Biochem* **84**, 131–164 (2015).
1332 53. Maison, C. & Almouzni, G. HP1 and the dynamics of heterochromatin
1333 maintenance. *Nat Rev Mol Cell Biol* **5**, 296–305 (2004).
1334 54. Probst, A. V. & Almouzni, G. Heterochromatin establishment in the
1335 context of genome-wide epigenetic reprogramming. *Trends in Genetics* **27**, 177–185 (2011).
1336 55. Heinz, S. *et al.* Simple Combinations of Lineage-Determining
1337 Transcription Factors Prime *cis*-Regulatory Elements Required for Macrophage and B Cell
1338 Identities. *Molecular Cell* **38**, 576–589 (2010).
1339 56. Chen, J., Kelz, M. B., Hope, B. T., Nakabeppu, Y. & Nestler, E. J. Chronic
1340 Fos-Related Antigens: Stable Variants of ΔFosB Induced in Brain by Chronic Treatments. *J.*

1341 *Neurosci.* **17**, 4933–4941 (1997).
1342 57. Herrup, K. & Yang, Y. Cell cycle regulation in the postmitotic neuron:
1343 oxymoron or new biology? *Nat Rev Neurosci* **8**, 368–378 (2007).
1344 58. Frost, B. Alzheimer's disease: An acquired neurodegenerative
1345 laminopathy. *Nucleus* **7**, 275–283 (2016).
1346 59. Mertens, J. *et al.* Age-dependent instability of mature neuronal fate in
1347 induced neurons from Alzheimer's patients. *Cell Stem Cell* **28**, 1533-1548.e6 (2021).
1348 60. Nagy, Z., Esiri, M. M., Cato, A.-M. & Smith, A. D. Cell cycle markers in
1349 the hippocampus in Alzheimer's disease. *Acta Neuropathologica* **94**, 6–15 (1997).
1350 61. Busser, J., Geldmacher, D. S. & Herrup, K. Ectopic Cell Cycle Proteins
1351 Predict the Sites of Neuronal Cell Death in Alzheimer's Disease Brain. *J. Neurosci.* **18**, 2801–
1352 2807 (1998).
1353 62. Vincent, I., Jicha, G., Rosado, M. & Dickson, D. W. Aberrant Expression
1354 of Mitotic Cdc2/Cyclin B1 Kinase in Degenerating Neurons of Alzheimer's Disease Brain. *J.*
1355 *Neurosci.* **17**, 3588–3598 (1997).
1356 63. Yang, Y., Mufson, E. J. & Herrup, K. Neuronal Cell Death Is Preceded by
1357 Cell Cycle Events at All Stages of Alzheimer's Disease. *J. Neurosci.* **23**, 2557–2563 (2003).
1358 64. Nagy, Z. & Esiri, M. M. Neuronal cyclin expression in the hippocampus
1359 in temporal lobe epilepsy. *Exp Neurol* **150**, 240–247 (1998).
1360 65. Hernández-Ortega, K. & Arias, C. ERK activation and expression of
1361 neuronal cell cycle markers in the hippocampus after entorhinal cortex lesion. *Journal of*
1362 *Neuroscience Research* **90**, 2116–2126 (2012).
1363 66. Pavlova, T., Stepanichev, M. & Gulyaeva, N. Pentylenetetrazole kindling
1364 induces neuronal cyclin B1 expression in rat hippocampus. *Neuroscience Letters* **392**, 154–158
1365 (2006).
1366 67. Love, S. Neuronal expression of cell cycle-related proteins after brain
1367 ischaemia in man. *Neuroscience Letters* **353**, 29–32 (2003).
1368 68. Jordan-Sciutto, K. L., Wang, G., Murphey-Corb, M. & Wiley, C. A. Cell
1369 Cycle Proteins Exhibit Altered Expression Patterns in Lentiviral-Associated Encephalitis. *J.*
1370 *Neurosci.* **22**, 2185–2195 (2002).
1371 69. Frost, B., Bardai, F. H. & Feany, M. B. Lamin dysfunction mediates
1372 neurodegeneration in tauopathies. *Current Biology* **26**, 129–136 (2016).
1373 70. Ogawa, O. *et al.* Ectopic localization of phosphorylated histone H3 in
1374 Alzheimer's disease: a mitotic catastrophe? *Acta Neuropathol* **105**, 524–528 (2003).
1375 71. Evangelisti, C. *et al.* The wide and growing range of lamin B-related

1376 diseases: from laminopathies to cancer. *Cell. Mol. Life Sci.* **79**, 126 (2022).
1377 72. Ripke, S. *et al.* Biological insights from 108 schizophrenia-associated
1378 genetic loci. *Nature* **511**, 421–427 (2014).
1379 73. Trubetskoy, V. *et al.* Mapping genomic loci implicates genes and synaptic
1380 biology in schizophrenia. *Nature* **604**, 502–508 (2022).
1381 74. Cascella, N. G., Schretlen, D. J. & Sawa, A. Schizophrenia and epilepsy:
1382 Is there a shared susceptibility? *Neuroscience Research* **63**, 227–235 (2009).
1383 75. Adachi, N. & Ito, M. Epilepsy in patients with schizophrenia:
1384 Pathophysiology and basic treatments. *Epilepsy & Behavior* **127**, 108520 (2022).
1385 76. Vossel, K. A., Tartaglia, M. C., Nygaard, H. B., Zeman, A. Z. & Miller, B.
1386 L. Epileptic activity in Alzheimer's disease: causes and clinical relevance. *The Lancet*
1387 *Neurology* **16**, 311–322 (2017).
1388 77. Targa Dias Anastacio, H., Matosin, N. & Ooi, L. Neuronal
1389 hyperexcitability in Alzheimer's disease: what are the drivers behind this aberrant phenotype?
1390 *Transl Psychiatry* **12**, 1–14 (2022).
1391 78. Frade, J. M. & Ovejero-Benito, M. C. Neuronal cell cycle: the neuron itself
1392 and its circumstances. *Cell Cycle* **14**, 712–720 (2015).
1393 79. Walton, C. C. *et al.* Primary neurons can enter M-phase. *Scientific Reports*
1394 **9**, 4594 (2019).
1395 80. Poleshko, A. *et al.* H3K9me2 orchestrates inheritance of spatial
1396 positioning of peripheral heterochromatin through mitosis. *eLife* **8**, e49278 (2019).
1397 81. Nestler, E. J., Barrot, M. & Self, D. W. ΔFosB: A sustained molecular
1398 switch for addiction. *Proceedings of the National Academy of Sciences* **98**, 11042–11046
1399 (2001).
1400 82. Nestler, E. J. Molecular basis of long-term plasticity underlying addiction.
1401 *Nat Rev Neurosci* **2**, 119–128 (2001).
1402 83. Corbett, B. F. *et al.* ΔFosB Regulates Gene Expression and Cognitive
1403 Dysfunction in a Mouse Model of Alzheimer's Disease. *Cell Reports* **20**, 344–355 (2017).
1404 84. Pande, G., Kumar, N. A. & Manogaran, P. S. Flow cytometric study of
1405 changes in the intracellular free calcium during the cell cycle. *Cytometry* **24**, 55–63 (1996).
1406 85. Borowiec, A.-S. *et al.* Calcium channels, external calcium concentration
1407 and cell proliferation. *European Journal of Pharmacology* **739**, 19–25 (2014).
1408 86. Yun, S. *et al.* Stimulation of entorhinal cortex–dentate gyrus circuitry is
1409 antidepressive. *Nature Medicine* **24**, 658–666 (2018).
1410 87. Tunc-Ozcan, E. *et al.* Activating newborn neurons suppresses depression

1411 and anxiety-like behaviors. *Nat Commun* **10**, 3768 (2019).
1412 88. Sackeim, H. A. *et al.* The Cognitive Effects of Electroconvulsive Therapy
1413 in Community Settings | Neuropsychopharmacology. *Neuropsychopharmacology* **32**, 244–254
1414 (2007).
1415 89. O'Connor, M. *et al.* A Dissociation Between Anterograde and Retrograde
1416 Amnesia After Treatment With Electroconvulsive Therapy: A Naturalistic Investigation. *The*
1417 *Journal of ECT* **24**, 146 (2008).
1418 90. Shepherd, J. D. *et al.* Arc/Arg3.1 Mediates Homeostatic Synaptic Scaling
1419 of AMPA Receptors. *Neuron* **52**, 475–484 (2006).
1420 91. Turrigiano, G. Homeostatic Synaptic Plasticity: Local and Global
1421 Mechanisms for Stabilizing Neuronal Function. *Cold Spring Harb Perspect Biol* **4**, (2012).
1422 92. Okuno, H. *et al.* Inverse Synaptic Tagging of Inactive Synapses via
1423 Dynamic Interaction of Arc/Arg3.1 with CaMKIIβ. *Cell* **149**, 886–898 (2012).
1424 93. Rotenberg, A., Mayford, M., Hawkins, R. D., Kandel, E. R. & Muller, R.
1425 U. Mice Expressing Activated CaMKII Lack Low Frequency LTP and Do Not Form Stable
1426 Place Cells in the CA1 Region of the Hippocampus. *Cell* **87**, 1351–1361 (1996).
1427 94. Cacucci, F., Wills, T. J., Lever, C., Giese, K. P. & O'Keefe, J. Experience-
1428 Dependent Increase in CA1 Place Cell Spatial Information, But Not Spatial Reproducibility,
1429 Is Dependent on the Autophosphorylation of the α-Isoform of the Calcium/Calmodulin-
1430 Dependent Protein Kinase II. *J. Neurosci.* **27**, 7854–7859 (2007).
1431 95. Kitanishi, T. *et al.* Novelty-Induced Phase-Locked Firing to Slow Gamma
1432 Oscillations in the Hippocampus: Requirement of Synaptic Plasticity. *Neuron* **86**, 1265–1276
1433 (2015).
1434 96. Vetencourt, J. F. M. *et al.* The antidepressant fluoxetine restores plasticity
1435 in the adult visual cortex. *Science* **320**, 385–388 (2008).
1436 97. Hensch, T. K. & Bilimoria, P. M. Re-opening Windows: Manipulating
1437 Critical Periods for Brain Development. *Cerebrum* **2012**, (2012).
1438 98. Karpova, N. N. *et al.* Fear Erasure in Mice Requires Synergy Between
1439 Antidepressant Drugs and Extinction Training. *Science* **334**, 1731–1734 (2011).
1440 99. Branchi, I. The double edged sword of neural plasticity: Increasing
1441 serotonin levels leads to both greater vulnerability to depression and improved capacity to
1442 recover. *Psychoneuroendocrinology* **36**, 339–351 (2011).
1443 100. Alboni, S. *et al.* Fluoxetine effects on molecular, cellular and behavioral
1444 endophenotypes of depression are driven by the living environment. *Mol Psychiatry* **22**, 552–
1445 561 (2017).

1446 101. Brown, K. A. & Gould, T. D. Targeting metaplasticity mechanisms to
1447 promote sustained antidepressant actions. *Mol Psychiatry* 1–14 (2024) doi:10.1038/s41380-
1448 023-02397-1.
1449 102. Abraham, W. C. & Bear, M. F. Metaplasticity: the plasticity of synaptic
1450 plasticity. *Trends in Neurosciences* **19**, 126–130 (1996).
1451 103. Stephens, G. S. *et al.* Persistent ΔFosB expression limits recurrent seizure
1452 activity and provides neuroprotection in the dentate gyrus of APP mice. *Progress in*
1453 *Neurobiology* 102612 (2024) doi:10.1016/j.pneurobio.2024.102612.
1454 104. Deibler, R. W. & Kirschner, M. W. Quantitative Reconstitution of Mitotic
1455 CDK1 Activation in Somatic Cell Extracts. *Molecular Cell* **37**, 753–767 (2010).
1456 105. Sparta, D. R. *et al.* Construction of implantable optical fibers for long-term
1457 optogenetic manipulation of neural circuits. *Nat Protoc* **7**, 12–23 (2012).
1458 106. Cardin, J. A. *et al.* Targeted optogenetic stimulation and recording of
1459 neurons in vivo using cell-type-specific expression of Channelrhodopsin-2. *Nat Protoc* **5**, 247–
1460 254 (2010).
1461 107. Yoshimura, Y. *et al.* Involvement of T-type Ca2+ channels in the
1462 potentiation of synaptic and visual responses during the critical period in rat visual cortex.
1463 *European Journal of Neuroscience* **28**, 730–743 (2008).
1464 108. Hagihara, H., Toyama, K., Yamasaki, N. & Miyakawa, T. Dissection of
1465 hippocampal dentate gyrus from adult mouse. *J Vis Exp* (2009) doi:10.3791/1543.
1466 109. Keller, D., Erö, C. & Markram, H. Cell Densities in the Mouse Brain: A
1467 Systematic Review. *Frontiers in Neuroanatomy* **12**, (2018).
1468 110. Buenrostro, J. D., Giresi, P. G., Zaba, L. C., Chang, H. Y. & Greenleaf, W.
1469 J. Transposition of native chromatin for multimodal regulatory analysis and personal
1470 epigenomics. *Nat Methods* **10**, 1213–1218 (2013).
1471 111. Corces, M. R. *et al.* An improved ATAC-seq protocol reduces background
1472 and enables interrogation of frozen tissues. *Nat Methods* **14**, 959–962 (2017).
1473 112. Robinson, J. T. *et al.* Integrative genomics viewer. *Nat Biotechnol* **29**, 24–
1474 26 (2011).
1475 113. Senda, T., Iizuka-Kogo, A. & Shimomura, A. Visualization of the Nuclear
1476 Lamina in Mouse Anterior Pituitary Cells and Immunocytochemical Detection of Lamin A/C
1477 by Quick-freeze Freeze-substitution Electron Microscopy. *J Histochem Cytochem.* **53**, 497–
1478 507 (2005).
1479 114. Coffinier, C. *et al.* Deficiencies in lamin B1 and lamin B2 cause
1480 neurodevelopmental defects and distinct nuclear shape abnormalities in neurons. *MBoC* **22**,

4683–4693 (2011).

115. Shoji, H. & Miyakawa, T. Age-related behavioral changes from young to old age in male mice of a C57BL/6J strain maintained under a genetic stability program. *Neuropsychopharmacology Reports* **39**, 100–118 (2019).

116. Miyakawa, T. *et al.* Conditional calcineurin knockout mice exhibit multiple abnormal behaviors related to schizophrenia. *PNAS* **100**, 8987–8992 (2003).

117. Stamatakis, A. M. *et al.* Simultaneous Optogenetics and Cellular Resolution Calcium Imaging During Active Behavior Using a Miniaturized Microscope. *Frontiers in Neuroscience* **12**, (2018).

118. Skaggs, W. E., McNaughton, B. L. & Gothard, K. M. An Information-Theoretic Approach to Deciphering the Hippocampal Code. in *Advances in Neural Information Processing Systems 5* (eds. Hanson, S. J., Cowan, J. D. & Giles, C. L.) 1030–1037 (Morgan-Kaufmann, 1993).

119. Kropff, E., Carmichael, J. E., Moser, M.-B. & Moser, E. I. Speed cells in the medial entorhinal cortex. *Nature* **523**, 419–424 (2015).

120. A novel somatosensory spatial navigation system outside the hippocampal formation | Cell Research. https://www.nature.com/articles/s41422-020-00448-8.

121. Glaser, J. I. *et al.* Machine Learning for Neural Decoding. *eNeuro* **7**, (2020).

122. Tanaka, M. *et al.* Fascin in lamellipodia contributes to cell elasticity by controlling the orientation of filamentous actin. *Genes to Cells* **24**, 202–213 (2019).

Acknowledgments

We thank the members of the Miyakawa laboratory—Wakako Hasegawa, Chikako Ozeki, Tamaki Murakami, Yoko Kagami and Harumi Mitsuya—for technical assistance, and Hirotaka Shoji for critical input on the design of the Ca^{2+} imaging experiment. We are grateful to Akihiro Yamanaka (Nagoya University and the Chinese Institute for Brain Research) for technical advice on optogenetics. We thank A. Konno, H. Hirai, and the Viral Vector Core at the Gunma University Initiative for Advanced Research for producing AAV9 viral particles. We also acknowledge D. Weinberger and T. Hyde for providing the human DG RNA-seq data. We thank Dr. Charles Yokoyama for his valuable comments, discussions, and editing and for greatly improving our manuscript. This research was supported by the Program for Brain Mapping by Integrated Neurotechnologies for Disease Studies (Brain/MINDS) from Japan Agency for Medical Research and Development, AMED under Grant Number JP21dm0207111, Japan Society for the Promotion of Science (JSPS) Grant-in-Aid for Scientific Research on Innovative Areas (grant nos. JP16H06462), JSPS KAKENHI (grant nos. JP20H00522 and JP22K15204), and the Japan Agency for Medical Research and Development Strategic Research Program for Brain Science Grant JP18dm0107101.

Author Contribution Statement

T. Murano, K. Takao, and T. Miyakawa designed the experiments and analyses. T. Murano performed RNA-seq, ATAC-seq, histological analysis, in vivo genome editing experiments, and data analyses. T. Murano and K. Takao performed the behavioral experiments. T. Murano and Y. Takamiya performed the Ca^{2+} imaging experiments. M. Namihira and K. Katoh performed the STED microscopy observations. K. Tajinda and M. Matsumoto provided RNA-seq data of post-mortem DG of human patients. T. Murano prepared all the figures and wrote the manuscript. T. Miyakawa supervised all aspects of the study. All authors reviewed the manuscript.

Declaration of Interests

The authors declare no competing interests.